8-22-2016

# The Driver of the Carbon Isotope Minima During the Last Deglaciation: A Weakened Biological Pump or Enhanced Southern Ocean Circulation?

Melissa C. Cote
*University of Connecticut*, melissa.cote@uconn.edu

# The Driver of the Carbon Isotope Minima During the Last Deglaciation:

# A Weakened Biological Pump or Enhanced Southern Ocean Circulation?

Melissa Cynthia Cote

B.S., University of Connecticut, 2013

A Thesis

Submitted in Partial Fulfillment of the Requirements of the

Degree of Master of Science

At the

University of Connecticut

2016

APPROVAL PAGE

Masters of Science Thesis

The Driver of the Carbon Isotope Minima During the Last Deglaciation: A Weakened Biological Pump or Enhanced Southern Ocean Circulation?

Presented by

Melissa Cynthia Cote, B.S.

Major Advisor_____

David C. Lund

Associate Advisor_____

Julie Granger

Associate Advisor_____

Craig Tobias

University of Connecticut

2016

University of Connecticut

2016

# ACKNOWLEDGMENTS

This thesis owes its existence to the help, support, and encouragement of several people. I would first like to thank my major advisor, David Lund, for presenting me with the opportunity to evolve a minor research endeavor for low key days in the laboratory into a Master's thesis. I thank him for introducing me into the field of paleoceanography, showing me that it is not just a history lesson, but a valuable tool that can be applied when evaluating the future of our oceans and climate. Without his superb organizational skills and knack for uncovering trends in large datasets, this thesis would not be what it today.

I am indebted to those on my advisory committee, Julie Granger and Craig Tobias, both of whom played vital roles in my decision to continue with marine sciences after my undergraduate career. Without a recommendation from Julie, I would never have acquired the position of laboratory technician in Dave's lab, an act for which I am very grateful. I would like to thank Craig for introducing me to the concept of mass balancing, knowledge that has been and will remain invaluable to me.

I would specifically like to thank Jennifer Hertzberg who always answered any of my mindless questions with a smile and for her help with compiling temperature records and proofreading this thesis. Thank you to my additional proofreaders, Emily Seeley and Alison Krasnor, for your helpful suggestions and comments.

I am grateful for both the University of South Carolina and Woods Hole Oceanographic Institute for allowing me access to the sediment samples analyzed in this thesis. Specifically, Bob Thunell and his lab from the University of South Carolina and Ellen Roosen from WHOI for sampling and shipping the sediment samples. Additionally, I'd like to thank Lora Wingate and the stable isotope laboratory from the University of Michigan for analyzing my stable isotope samples and providing helpful information on their methodology.

The faculty and staff at the University of Connecticut, Avery Point, played essential roles in the timely completion of my graduate study. Specifically, Debra Schuler who is an ace at navigating the graduate program here at UConn, and was instrumental in providing me with the tools to complete my degree on a shortened time scale. I am very grateful for Todd Fake who guided me through the process of purchasing a new laptop when matlab became too much for my faithful 8-year-old MacBook Pro and additionally for setting me up with all the new software. Thank you to Pat Evans and Janet Laflamme for your speedy email responses and helping with shipping samples and purchasing lab materials.

Of course I would not be where I am today without the endless love and support from my parents. Thank you for always pushing me to accomplish more and forcing me out of my comfort zone. Christian Fox, I thank you for reminding that there is still a world outside of my computer screen and for always stubbornly challenging me, pushing me to procure an answer to what seems an unanswerable question.

Finally, I thank the University of Connecticut for funding the research utilized in this thesis.

TABLE OF CONTENTS

LIST OF FIGURES

LIST OF TABLES

ABSTRACT

The cause of the initial rise in atmospheric $CO_2$ during the last deglaciation remains unknown. Coincident with the rising atmospheric $CO_2$, the $\delta^{13}C$ of atmospheric $CO_2$ decreased by ~0.3‰ during Heinrich Stadial 1 (HS1: 14.5-17.5 kyr BP), which requires the input of carbon from an isotopically light reservoir. The light carbon signal in the atmosphere occurred concurrently with the carbon isotope minimum, or a decrease in surface ocean $\delta^{13}C$ of ~0.5‰, suggesting the two phenomena are related. The leading hypotheses explaining the $\delta^{13}C$ minimum are (1) enhanced ventilation of $^{13}C$-depleted abyssal water in the Southern Ocean which in turn caused low $\delta^{13}C$ values in the surface ocean and atmosphere, and (2) a reduction in the Atlantic Meridional Overturning Circulation (AMOC) weakened the efficiency of the ocean's biological pump, thereby increasing the concentration of light carbon in the surface ocean. In order to evaluate these two hypotheses, we compiled 70 published, globally-distributed planktonic foraminiferal $\delta^{13}C$ records and enhanced the sampling resolution of three low resolution records from the western tropical Pacific (WTP). The HS1 $\delta^{13}C$ anomaly, or the relative difference in $\delta^{13}C$ between the LGM and HS1, was calculated for each record, and we compared the spatial patterns between ocean basins and within the tropical Pacific and Southern Oceans. We find that the average $\delta^{13}C$ anomaly is similar in all ocean basins. We also find similar $\delta^{13}C$ signals in the eastern equatorial Pacific (EEP) upwelling regime and the WTP convergence zone. In the Southern Ocean we find a latitudinal trend of $\delta^{13}C$ anomalies decreasing in magnitude progressing towards higher latitudes and the region of abyssal upwelling. Because the Southern Ocean hypothesis implies that the $\delta^{13}C$ signal should be largest in the Southern Ocean and in upwelling regions, our results are inconsistent with a Southern Ocean driver. Our findings are instead consistent with a recent modeling study that simulated the effects of a weakened biological pump, which produced an excess of isotopically light carbon in the surface ocean and atmosphere, similar to observations. We conclude that our results are broadly consistent with a biological pump mechanism, suggesting that the initial rise in atmospheric $CO_2$ was driven by biogeochemical processes in the upper ocean as opposed to upwelling of light carbon from the abyss.

## 1. Introduction

a) Background

Atmospheric carbon dioxide ($CO_2$) fluctuated in step with glacial-interglacial cycles during the late Pleistocene. Atmospheric $pCO_2$ is lowest during glacial intervals, increases during glacial terminations, and peaks during interglacial periods, with a total dynamic range of 80-100 p.p.m.v. (Barnola et al., 1987; Petit et al., 1999). During the last deglaciation (10-18 kyr BP), rising $CO_2$ levels led the increase in global surface temperature, indicating that $CO_2$ is a key driver of glacial terminations (Shakun et al., 2012) and consistent with model simulations demonstrating that higher atmospheric $CO_2$ enhances global warming (e.g. Webb et al., 1997). Although the basic character of glacial-interglacial $CO_2$ cycles has been known for over 30 years (Neftel et al., 1982), their cause remains enigmatic (Sigman and Boyle, 2000; Sigman et al., 2010). Investigating the ultimate driver of atmospheric $CO_2$ variability is therefore important for understanding the cause of glacial terminations and the long-term behavior of the global carbon cycle.

At the onset of the last deglaciation, during an interval known as Heinrich Stadial 1 (HS1: 14.5-17.5 kyr BP), atmospheric $CO_2$ rose by 30 p.p.m.v. while the $\delta^{13}C$ of atmospheric $CO_2$ decreased by ~0.3‰ (Figure 1A, B) (Monnin et al., 2001; Schmitt et al., 2012; Veres et al., 2013, Bauska et al., 2016). Foraminiferal $\delta^{13}C$ records from the surface ocean show a decrease in $\delta^{13}C$ of dissolved inorganic carbon (DIC) during the same time period (e.g. Ninnemann and Charles, 1997; Curry et al., 1988; Schneider et al., 1992; Spero and Lea, 2002). The surface ocean anomalies, otherwise known as carbon isotope minima, are characterized by large, rapid negative excursions in surface ocean $\delta^{13}C$ during HS1 relative to the Last Glacial Maximum (LGM: 19-23 kyr BP) (Spero and Lea, 2002). Here I generate a stack of 21 high-resolution planktonic foraminiferal $\delta^{13}C$ records that clearly displays a ~0.5‰ decrease during HS1 (Figure 1C). The simultaneous timing of the negative $\delta^{13}C$ anomalies in the surface ocean and atmosphere during HS1 suggests the light carbon signals originated from the same $^{13}C$-depleted source. Further, the timing of the anomalies coincides with the onset of the atmospheric $CO_2$ rise (Figure 1). The

synchronicity of the atmospheric and surface ocean signals implies that the release of carbon from a $^{13}C$-depleted source initiated the last deglaciation. Thus, determining the cause of the surface ocean $\delta^{13}C$ minima is key to understanding the ultimate driver of glacial terminations.

It is unlikely that the light carbon originated from terrestrial reservoirs ($\delta^{13}C$ = -25‰). During the deglaciation, retreating glaciers allowed terrestrial biomass to accumulate in areas previously covered in ice. Because the terrestrial biosphere expanded and sequestered $^{12}C$-rich carbon into biomass, this would have the effect of driving the ocean and atmosphere to more positive $\delta^{13}C$ values, opposite the observed pattern (Spero and Lea, 2002). Instead, an oceanic mechanism is more likely, the exact nature of which is discussed in detail in the following sections.

Deglacial carbon isotope minima occurred in the Pacific, Atlantic, Indian, and Southern Oceans. Individual studies suggest that surface ocean $\delta^{13}C$ decreased ~0.5‰ in the eastern equatorial Pacific (EEP) (Spero and Lea, 2002), southwest Pacific (Bostock et al., 2004), Indian Ocean (Kiefer et al., 2006) and Southern Ocean (Carter et al., 2008; Charles et al., 1996), as well as up to -1‰ in the eastern tropical Atlantic (Schneider et al., 1992). The rapid rate at which the $\delta^{13}C$ anomalies occurred in various ocean basins requires a mechanism that can simultaneously influence all regions of the ocean (Ninnemann and Charles, 1997). Although carbon isotope minima appear in many planktonic $\delta^{13}C$ records, there has been no attempt to systematically compile records from a range of locations and assess spatial patterns or signal dependence on planktonic foraminiferal species. The lack of such a study has precluded testing of hypotheses, and therefore allowed the prevailing Southern Ocean view to remain fixed in the collective conscientiousness of the paleo-community.

b) Southern Ocean Hypothesis

The primary explanation that has been used to account for surface ocean $\delta^{13}C$ minima is known as the Southern Ocean hypothesis. In this scenario, the low $\delta^{13}C$ signal originated from enhanced ventilation of a $^{13}C$-depleted abyssal water mass in the Southern Ocean, which was then advected to lower latitudes

via Antarctic Intermediate Water (AAIW) and sub-Antarctic Mode Water (SAMW) and brought to the surface ocean through upwelling of these water masses (Spero and Lea, 2002). Spero and Lea (2002) based their idea on the premise that isotopically light carbon accumulated in the deep ocean during the last glacial period only to be released early in the deglaciation. Studies showing that abyssal waters accumulated light carbon ($^{12}C$) during the LGM, potentially as a result from increased stratification (Toggweiler et al., 2006) or an enhanced biological pump (Broecker, 1982) formed the basis for the Southern Ocean hypothesis.

While providing a source of $^{13}C$-depleted carbon and a means to globally transport the low $\delta^{13}C$ signal, there is conflicting evidence for intensified abyssal circulation at the onset of the deglaciation. Surface ocean productivity records appear to be consistent with increased upwelling resulting from a poleward shift in the Southern Hemisphere westerly winds during the deglaciation (Anderson et al., 2009; Toggweiler, 1999; Toggweiler et al., 2006). Additionally, a recent synthesis inferred changes in wind patterns using proxies for terrestrial moisture, dust deposition, sea surface temperature (SST), ocean fronts, productivity, and ocean circulation (Kohfeld et al., 2013). The results were inconclusive, however, as the observations can support either an overall strengthening in the westerly winds, an equatorward displacement, or no change at all (Kohfeld et al., 2013). Paleo data and climate models, therefore, do not provide clear evidence for a change in the westerly wind belt during the deglaciation. Further, several modeling studies demonstrate that a shift in the Southern Hemisphere westerlies could not produce a rise in atmospheric $CO_2$ similar to that recorded in ice cores (Tschumi et al., 2008; Menviel et al., 2008; d'Orgeville et al., 2010; Volker and Kohler, 2013).

A recent study demonstrated that enhanced upwelling in the Southern Ocean was unlikely the source of isotopically light carbon during HS1. Using benthic foraminiferal $\delta^{13}C$ and $\delta^{18}O$ reconstructions along a depth transect, the study revealed that the abyssal water mass below 3 km remained isotopically light until ~15 kyr BP, suggesting abyssal circulation changed well after the occurrence of surface ocean $\delta^{13}C$ anomalies and the initial increase in atmospheric $CO_2$ (Lund et al.,

2015). Above 3 km, negative mid-depth $\delta^{13}C$ anomalies found from 1.3-2.5 km are likely driven by a weakened Atlantic Meridional Overturning Circulation (AMOC) (Lund et al., 2015; Oppo et al., 2015). The lack of support from modeling results and isotopic records suggests another mechanism besides enhanced Southern Ocean circulation is required to explain the carbon isotope minima, and thus the initial rise in atmospheric $CO_2$.

c) Biological Pump Hypothesis

When investigating carbon isotopes in the ocean, one must first understand how the biological pump, the primary influence on $\delta^{13}C$ in the ocean, sets the overall $\delta^{13}C$ depth structure. High $\delta^{13}C$ in the surface ocean and low $\delta^{13}C$ deeper in the water column characterizes a typical depth profile of the $\delta^{13}C$ of DIC (Figure 2). Photosynthesis utilizes nutrients and carbon in the surface ocean, preferring $^{12}C$ to $^{13}C$, as the lighter isotope is more easily assimilated by the biota. Thus, photosynthetic organisms leave the surface waters high in $\delta^{13}C$. As organic matter sinks, remineralization releases inorganic nutrients and $^{12}C$, establishing lower $\delta^{13}C$ values deeper in the water column. The combination of photosynthesis in the surface ocean and respiration at depth results in an inverse relationship between inorganic nutrients, such as phosphate, and $\delta^{13}C$ (Figure 2) (Kroopnick, 1985).

Rather than invoking outgassing of isotopically light carbon from the abyssal ocean, recent studies suggest that a weakening of the AMOC can produce synchronous surface ocean $\delta^{13}C$ anomalies in multiple ocean basins (Schmittner and Lund, 2015; Lund et al., 2015). In essence, a reduction of the AMOC decreases the efficiency of the biological pump by altering the balance between preformed and regenerated nutrients in the global ocean.

The relative concentration of preformed to regenerated nutrients in the global ocean dictates the overall efficiency of the biological pump (Ito and Follows, 2005). Surface waters traveling north through the Atlantic are stripped of nutrients and $^{12}C$ due to photosynthesis. Upon reaching the North Atlantic, where they sink and form North Atlantic Deep Water (NADW), the surface waters are low in preformed

nutrients (i.e. nutrients unused by photosynthesis) and have a high $\delta^{13}C$ of DIC (Kroopnick, 1985; Ito and Follows, 2005). The low fraction of preformed nutrients in NADW indicates efficient operation of the biological pump and sequestration of carbon in the abyss. In contrast, Antarctic Bottom Water (AABW) has a high concentration of preformed nutrients because the residence time of upwelled deep water in the surface of the Southern Ocean is too short for biological productivity to utilize the nutrient-rich water (Ito and Follows, 2005). After upwelling, the nutrient-rich waters are quickly subducted, forming AABW, AAIW, and SAMW. The Southern Ocean circulation therefore represents an inefficient or a missed opportunity for the biological pump to sequester $CO_2$ to the deep ocean (Ito and Follows, 2005). Because of the relationship between the concentration of preformed nutrients and the efficiency of the biological pump, we can relate preformed nutrient content to atmospheric $CO_2$ concentrations.

Both theory and modeling results suggest there is a nearly linear relationship between the fraction of preformed nutrients in the ocean and atmospheric $CO_2$ (Ito and Follows, 2005) (Figure 3). An efficient biological pump and lower fraction of preformed nutrients (a NADW-centric circulation) results in more atmospheric $CO_2$ sequestered into the deep ocean and therefore lower atmospheric $pCO_2$ (Figure 3). When the biological pump is inefficient (i.e. an AABW-centric circulation), the opposite occurs. During HS1, a weakened AMOC may have reduced the fraction of NADW in the deep ocean, increasing the global fraction of preformed nutrients and therefore limiting the overall efficiency of the biological pump (Schmittner and Lund, 2015). Thus, weakening of the AMOC may have caused atmospheric $CO_2$ levels to increase during HS1.

Early theory suggests the AMOC is capable of multiple steady states with potentially rapid transitions (Stommel, 1961). General circulation models show that adding fresh water into the North Atlantic results in a substantial weakening of the AMOC (Schmittner and Lund, 2015; Bouttes et al., 2011; Schmittner and Galbraith, 2008; Obata, 2007). $^{231}Pa/^{230}Th$ ratios signifying a possible collapse of the AMOC around 18-19 kyr BP coincide with the initiation of the atmospheric $CO_2$ rise during the onset of the last deglaciation (McManus et al., 2004; Shakun et al., 2012; Chen et al., 2015). However, more

recent $^{231}Pa/^{230}Th$, $\delta^{13}C$, and $\delta^{18}O$ records indicate a total collapse is unlikely, but rather a significant reduction in the overturning circulation took place (Gherardi et al., 2009; Lund et al., 2015; Oppo et al., 2015).

d) Model of Ocean Biogeochemistry and Isotopes (MOBI 1.4)

Recent modeling results simulating the collapse of the AMOC demonstrate how changes in the overturning circulation and the biological pump may affect atmospheric and oceanic $\delta^{13}C$. Using the Model of Ocean Biogeochemistry and Isotopes (MOBI 1.4) coupled to the University of Victoria intermediate complexity ocean general circulation model, Schmittner and Lund (2015) (SL15 from here on) simulated perturbations in the AMOC using four different freshwater forcing events in the North Atlantic. The two larger forcings, 0.15 Sv (1 Sv = $10^6$ $m^3$ $s^{-1}$) and 0.2 Sv, result in a nearly complete shutdown of the AMOC and yield a rise in atmospheric $CO_2$ similar to ice core records during HS1 (Monnin et al., 2001; Marcott et al., 2014). Additionally, the model results suggest that the $\delta^{13}C$ of atmospheric $CO_2$ decreases by ~0.3‰, also consistent with ice core measurements (Marcott et al., 2014; Schmitt et al., 2012). An AMOC collapse increases preformed $PO_4$ in the global ocean, reflecting an overall weakening biological pump, and the accumulation of carbon in the surface ocean and atmosphere (Schmittner, 2005).

The resulting spatial map of oceanic $\delta^{13}C$ anomalies from the 0.15 Sv forcing (Figure 4) is similar to deep Atlantic $\delta^{13}C$ observations during HS1 (Lund et al., 2015; Schmittner and Lund, 2015; Oppo et al., 2015). Reducing the overturning circulation in the model yields very larger $\delta^{13}C$ anomalies in the mid-depth North Atlantic (~ -1‰) that are a direct result of the weakened AMOC (Figure 4). Essentially, the reduced overturning limits sinking of high $\delta^{13}C$ surface waters in the North Atlantic, decreasing the $\delta^{13}C$ of NADW. The weakened circulation also increases the residence time of deep water in the North Atlantic, allowing for the accumulation of isotopically light respired carbon (Schmittner and Lund, 2015). Benthic $\delta^{13}C$ records from 1-2 km the Atlantic show a meridional gradient in the $\delta^{13}C$ anomalies, with the

largest signal in the North Atlantic and progressively smaller anomalies in the tropical and South Atlantic. This trend is consistent with the SL15 modeling results, therefore supporting a weakened AMOC during HS1 (Oppo et al., 2015).

The 0.15 Sv forcing generally results in negative surface ocean $\delta^{13}C$ anomalies, with a range in minima of -0.2‰ to -0.4‰ in the Pacific, Indian, and South Atlantic. The negative surface ocean minima are a result of the weakened biological pump and subsequent nutrient budget. There is a mixed spatial signal in the North Atlantic, with both positive and negative anomalies, due to the combination of the direct impact of the AMOC collapse in the North Atlantic and weakened biological pump. In the Southern Ocean, the SL15 simulation results in a latitudinal trend of negative $\delta^{13}C$ anomalies decreasing in magnitude moving south and ultimately switching signs at ~60°S. Positive anomalies in the Southern Ocean at latitudes higher than ~60°S result from upwelling of isotopically heavy carbon at intermediate depths in the Pacific, Indian, and South Atlantic due to reduced export production.

e) Evaluating the Southern Ocean and Biological Pump Hypotheses

The Southern Ocean and biological pump mechanisms would produce different spatial patterns in oceanic $\delta^{13}C$ during HS1. According to the Southern Ocean hypothesis, we would expect to find negative $\delta^{13}C$ anomalies of larger magnitude in the Southern Ocean, where upwelling of the low $\delta^{13}C$ abyssal water mass occurs. Likewise, $\delta^{13}C$ anomalies would be larger in areas where AAIW and SAMW reside and where upwelling of these water masses occurs (Spero and Lea, 2002). In regions outside of upwelling zones, mixing with surface waters would dilute the low $\delta^{13}C$ signal, producing $\delta^{13}C$ anomalies of smaller magnitude. According to the biological pump hypothesis, the sea surface $\delta^{13}C$ anomalies would be of similar magnitude in multiple locations. Additionally, we would expect slightly muted anomalies in upwelling regimes due to positive $\delta^{13}C$ anomalies at intermediate depths. By compiling planktonic foraminiferal $\delta^{13}C$ records we can assess spatial patterns in $\delta^{13}C$ anomalies and determine whether they are consistent with the Southern Ocean or biological pump mechanisms.

## 2. Methods

a) Published Planktonic $\delta^{13}C$ Records

We compiled 70 published planktonic foraminiferal $\delta^{13}C$ records to determine the magnitude and spatial trends in carbon isotope minima. The records are categorized into one of four tiers based on the quality of the data. The highest quality records are Tier 1 while the lowest quality data are Tier 4. We evaluate the quality of the data using three criteria: the coherency of the $\delta^{18}O$ stratigraphy, the sampling resolution, and whether or not the age model is constrained by radiocarbon dates.

A coherent $\delta^{18}O$ stratigraphy is the first criterion used in assessing the fidelity of a given sediment core, verifying the structural integrity. The $\delta^{18}O$ stratigraphy of each core was compared to the global benthic foraminiferal $\delta^{18}O$ stack (Lisiecki and Raymo, 2005) that records the Earth's transitions from glacial to interglacial states. As we are mainly interested in the last deglaciation, each core must show a $\delta^{18}O$ transition from the LGM to the Holocene similar to that observed in the global stack. Records without a coherent $\delta^{18}O$ stratigraphy were considered Tier 4 (28 total cores) and their data were not included in this compilation. Therefore, all 70 cores compiled here met the basic requirement of a coherent $\delta^{18}O$ stratigraphy.

All of the $\delta^{13}C$ records in this compilation have a clear $\delta^{18}O$ stratigraphy, however, many of the records ($n = 27$) have a low sampling resolution of $< 1$ data point per kyr and were assigned to Tier 3. A high sampling resolution is necessary in order to capture the full magnitude of millennial-scale $\delta^{13}C$ anomalies in each record. Both Tier 1 and Tier 2 records have a high sampling resolution of $> 1$ sample per kyr.

In addition to a clear $\delta^{18}O$ stratigraphy and a sampling resolution of $> 1$ data point per kyr, Tier 1 $\delta^{13}C$ records have an age model generated using radiocarbon dates. Radiocarbon dates typically have an age error of $\pm 1$ kyr, while age models based on oxygen isotope control points have an error of $\pm 3$ kyr.

Radiocarbon-based age models therefore provide more confidence in the timing of $\delta^{13}C$ minima than records with age models based only on their $\delta^{18}O$ stratigraphy.

To summarize, Tier 1 records each have a coherent $\delta^{18}O$ stratigraphy, a sampling resolution of > 1 sample per kyr, and an age model constrained by radiocarbon dates. Tier 2 records have a coherent $\delta^{18}O$ stratigraphy and a high sampling resolution (> 1 sample per kyr), while Tier 3 records only have a coherent $\delta^{18}O$ stratigraphy. Records lacking a clear $\delta^{18}O$ stratigraphy were placed into Tier 4 (28 cores total) and were not included in the compilation.

*i. Age Models*

All radiocarbon dates for Tier 1 age models were recalibrated using Calib 7.1 (http://calib.qub.ac.uk/calib/). Surface water reservoir ages were calculated using the marine reservoir correction database (http://calib.qub.ac.uk/marine/) to determine regional offsets ($\Delta R$) from the global value of 400 years (R). The marine reservoir correction database calculates $\Delta R$ as the difference between the $^{14}C$ age of known-age, pre-nuclear marine samples and the marine calibration dataset (Reimer et al., 2004). $\Delta R$ for each Tier 1 core is an average of the 10 closest $\Delta R$ values listed in the database, excluding any values that are farther than 1 km from the location of the core (Table A1). An error of ±200 years was applied to each $\Delta R$ value.

A sediment core's $\delta^{18}O$ stratigraphy forms the basis for Tier 2 and Tier 3 age models. A majority of the published age models are based on oxygen control points that are established between the well-dated global benthic $\delta^{18}O$ stack and the $\delta^{18}O$ record at glacial/interglacial transitions. We re-evaluated each published age model by comparing the existing $\delta^{18}O$ stratigraphy to the global benthic $\delta^{18}O$ stack (Lisiecki and Raymo, 2005). In cases where the published age model did not correspond well with the global stack or the records did not already have an age model, a new age model was generated. Control points at the LGM to Holocene transition (~15 kyr BP), or the Marine Isotope Stage (MIS) 2/1 boundary, were determined in the $\delta^{18}O$ stratigraphy. In cases where a $\delta^{18}O$ stratigraphy was long enough, additional

control points were established at the relevant MIS boundaries. We assumed the top of each core has an age of 0 kyr BP. Linear interpolation was used to determine ages between the $\delta^{18}O$-based control points.

*ii. Vital Effects*

Biological processes, such as foraminiferal respiration, photosynthetic fractionation by algal symbionts, vertical migration, and environmental influences, such as seawater carbonate ion concentrations, can influence the $\delta^{13}C$ of DIC in seawater immediately surrounding a foraminifer (Curry and Crowley, 1987; Spero and Lea, 1993, 1996; Spero et al., 1997; Spero et al., 2003). These 'vital' effects can alter the carbon isotopic composition of the foraminiferal test, shifting shell $\delta^{13}C$ away from isotopic equilibrium, creating an offset between the $\delta^{13}C$ of calcite and $\delta^{13}C$ of DIC ($\Delta\delta^{13}C_{shell\text{-}DIC}$). To determine species-specific $\delta^{13}C$ offsets, plankton tows have been used to collect foraminifera and compare the $\delta^{13}C$ of their shells to the $\delta^{13}C_{DIC}$ of the seawater in which they inhabited. For example, Spero et al. (2003) found the $\Delta\delta^{13}C_{shell\text{-}DIC}$ for *Globigerinoides sacculifer* is $+0.73 \pm 0.23$‰ (1SE) in the eastern equatorial Pacific (EEP). Because we are mainly interested in anomalies from the LGM to HS1 in the $\delta^{13}C$ records instead of actual sea surface $\delta^{13}C_{DIC}$ values, species-specific $\delta^{13}C$ offsets were not applied in this study.

To account for potential vital effects, the planktonic foraminifera $\delta^{13}C$ compilation includes multiple species that appear to reliably record the $\delta^{13}C$ of DIC through time. The compilation includes species with and without symbionts and those that dwell in the surface mixed layer and thermocline depths. For the surface mixed layer, we used $\delta^{13}C$ records from the symbiont-bearing *G. sacculifer* (Curry and Crowley, 1987; Spero et al., 2003) and non-symbiont bearing *Globigerina bullodies* (Ninnemann and Charles, 1997). Non-symbiont bearing *Globorotalia inflata* (Pierre et al., 2001; Carter et al., 2008) and symbiont bearing species *Neogloboquadrina dutertrei* (Spero and Lea, 2002; Spero et al., 2003) and *Globorotalia menardii* (Spero et al., 2003) were used to characterize thermocline depths. Using a multi-species approach that incorporates the diversity between species (i.e. symbiont/non-symbiont and depth habitat) minimizes potential biases associated with vital effects.

b) Determining $\delta^{13}C$ Anomalies

We calculated $\delta^{13}C$ anomalies using raw planktonic foraminifera $\delta^{13}C$ datasets collected from the literature and online databases PANGAEA (pangaea.de) and the National Climatic Data Center (ncdc.noaa.gov). Anomalies are used in order to control for any mean $\delta^{13}C$ offsets between species and oceanographic settings. For each record, we use an average LGM value computed from $\delta^{13}C$ data between 19 and 23 kyr BP. Maximum anomalies are calculated as the difference between the average LGM value and the lowest $\delta^{13}C$ value during the deglaciation (12 to 18 kyr BP). To account for potential biases associated with one point outliers, we also applied a 3-point running mean to each record. Running mean anomalies represent the difference between the averaged LGM value and the minimum $\delta^{13}C$ value in the 3-point running mean selected between 12 and 18 kyr BP. The timeframe for selecting minimum $\delta^{13}C$ values is broader than the HS1 time interval (14.5-17.5 kyr BP) in order to account for age uncertainty in each $\delta^{13}C$ record. Tier 2 and Tier 3 age models based on $\delta^{18}O$ stratigraphies may have age errors of up to 3 kyr, while the radiocarbon-based age models for the Tier 1 cores have age uncertainties of ~1 kyr. The sensitivity of our compilation to the choice of age window is discussed in the results section.

c) Stacking Tier 1 Data sets

We generated the planktonic $\delta^{13}C$ stack by first interpolating each of the Tier 1 records (n = 21) at a 600-year increments, which is the average resolution for the Tier 1 records. The mean $\delta^{13}C$ of each record was then subtracted from each time series to facilitate comparison across species and oceanographic settings. Unlike normalization, which would have created records in units of standard deviation ($\sigma$), we used the mean adjusted approach so that the resulting time series would retain $\delta^{13}C$ units (‰). The stacked $\delta^{13}C$ time series was created by simply averaging the mean-adjusted records.

d) Temperature Records

We compiled published temperature records in order to account for the potential influence of sea surface temperature on air-sea fractionation of carbon isotopes. Equilibrium fractionation occurs between surface ocean DIC (DIC = $CO_{2aq}$ + $HCO_3^-$ + $CO_3^{2-}$) and atmospheric $CO_2$ (Broecker and Maier-Reimer, 1992; Lynch-Stieglitz et al., 2005). During this process, each DIC species must exchange with atmospheric $CO_2$ in order to reach isotopic equilibrium, a process that takes ~10 years (Broecker and Peng, 1974). Fractionation of carbon isotopes during air-sea gas exchange increases with decreasing temperatures, producing a thermodynamic slope where surface water $\delta^{13}C$ of DIC increases 0.1‰ with every 1°C decrease in temperature (Broecker and Maier-Reimer, 1992). Therefore, at isotopic equilibrium colder waters have higher $\delta^{13}C$ values than warmer waters.

Shakun et al. (2012) compiled SST records created using various proxies over the last deglaciation. The age model for each record is based on radiocarbon dates and each time series has a resolution of > 1 sample per kyr. We focused on Mg/Ca-based temperature records given the large number of available sites and the reproducibility of Mg/Ca-based SSTs. Additional Mg/Ca records with radiocarbon-based age models and high sample resolution were added for a more robust global compilation (Pena et al., 2008; Johnstone et al., 2014; Zarriess et al., 2011; Chiessi et al., 2015; Martinez-Mendez et al., 2010; Pahnke et al., 2003; Romahn et al., 2014; Govil and Naidu, 2010). Mg/Ca-derived SSTs from each source were interpolated to a 100-year resolution, following Shakun et al. (2012). Because the rate of temperature rise varied by location (Shakun et al., 2012), we accounted for regional biases by grouping the temperature records by location. Temperature records were organized by latitude and classified as either sub-polar, sub-tropical, or tropical. Within those sections, the regions were further categorized by more distinct oceanographic regions, with some regions represented by only one record. In cases where more than one record existed for a region they were averaged together. Using an LGM value computed from temperatures averaged from 19-23 kyr BP and a HS1 temperature value averaged from 14.5-17.5 kyr BP, we estimated the deglacial rise in SST for each region as the difference between the mean LGM value and the mean HS1 value.

e) New Planktonic Stable Isotope Records

The limited number of Tier 1 and 2 records in the literature makes it difficult to assess spatial patterns in the $\delta^{13}C$ anomalies. In particular, the paucity of high quality records from the western tropical Pacific (WTP) made it necessary to improve existing Tier 3 records from that region. Three cores were selected for resampling in order to improve their resolution to > 1 point per kyr. GGC10 (11.93°N, 118.21°E), GGC13 (11.89°N, 118.21°E), and MW91-9-15 (14.53°S, 157.98°E) are all located in the WTP and were available for resampling at the University of South Carolina (GGC10 and GGC13) and the Woods Hole Oceanographic Institution (MW91-9-15).

Intervening depths for sampling were selected based on sedimentation rates estimated from the core age model. New age models were established for GGC10 and GGC13 based on their individual $\delta^{18}O$ stratigraphies as previously outlined (see Methods). We assumed a constant sedimentation rate between the $\delta^{18}O$ control points to establish updated age models. Sampling depths were chosen such that the final sampling resolution of each record was > 1 sample per kyr. Despite having three available radiocarbon dates, core MW91-9-15 is considered a Tier 3 core due to its low sampling resolution. The age model for MW91-9-15 was updated using the same approach as the Tier 1 age models (see Methods). We assumed a constant sedimentation rate between each calibrated radiocarbon date in the revised age model. Intervening depths for sampling were chosen in order to increase the final sampling resolution to > 1 data point per kyr.

Each sediment sample for the three cores was frozen, freeze-dried, and washed through a 150 μm sieve in order to isolate the size fraction containing foraminifera. We used the planktonic foraminifera *G. sacculifer* to match the species used in the earlier studies (Thunell et al., 1992; Patrick and Thunell, 1997). For each depth, 6-8 foraminiferal tests were picked from the 300-355 μm size fraction after Curry and Crowley (1987). Individuals with a terminal sac were avoided to account for potential biases associated with gametogenic calcite (Curry and Crowley, 1987). Stable isotope analyses for $\delta^{13}C$ and $\delta^{18}O$ were performed on a Finnigan MAT 253 isotope ratio mass spectrometer (IRMS) coupled to a Kiel

IV automated carbonate device at the Stable Isotope Laboratory at the University of Michigan. The data (n = 45) were converted to Vienna Pee Dee Belemnite using NBS-19 (National Institute of Standards and Technology, USA) ($\delta^{18}O$ = -2.22 ± 0.05‰ (1SE), n = 13; $\delta^{13}C$ = 1.95 ± 0.03‰ (1SE), n = 13).

**3. Results**

a) Global $\delta^{13}C$ Anomalies

The global Tier 1 $\delta^{13}C$ stack shows a 0.5‰ decrease in surface ocean $\delta^{13}C$ from the LGM to HS1, reaching a minimum value at ~15.5 kyr BP (Figure 1C). The magnitude of the global $\delta^{13}C$ anomalies decreases with lower quality records, likely due to the greater sampling resolution of the higher quality Tier 1 and Tier 2 data (Figure 5). For Tier 1 minima, the average maximum $\delta^{13}C$ anomaly is -0.57 ± 0.10‰ (1SE) and the average running mean anomaly is -0.47 ± 0.09‰ (1SE). By comparison, the Tier 2 data yield a maximum anomaly of -0.47 ± 0.06‰ (1SE) and a running mean anomaly of -0.33 ± 0.05‰ (1SE). Thus, the Tier 2 data yield a smaller signal but remain within one standard error of the Tier 1 values. However, the Tier 3 data have a maximum anomaly of -0.38 ± 0.04‰ (1SE) and a running mean $\delta^{13}C$ anomaly of -0.20 ± 0.03‰ (1SE), clearly distinct from the Tier 1 results. The smaller Tier 3 signal is due to the lower sampling resolution, increasing the likelihood that the full magnitude of the $\delta^{13}C$ signal isn't captured in these records (see Methods). The relationship between tier and the magnitude of the $\delta^{13}C$ minima demonstrates the importance of having high quality $\delta^{13}C$ records for assessing $\delta^{13}C$ minima during HS1.

b) Basin-scale $\delta^{13}C$ Anomalies

The locations and corresponding tier for each $\delta^{13}C$ record are displayed in Figure 6 and the average $\delta^{13}C$ anomaly for each ocean basin is shown in Table 1. Overall, there is a remarkable degree of homogeneity in the results, with statistically similar $\delta^{13}C$ anomalies regardless of ocean basin. Ranging from -0.4‰ to -0.5‰, the average maximum $\delta^{13}C$ anomalies of each ocean basin are within 1SE of one another (Table 1). In each ocean basin the magnitude of the running mean anomalies is generally ~0.1‰

smaller than the maximum $\delta^{13}C$ signal, primarily due to the smoothed nature of the running mean time series (Table 1).

**Table 1. Regional running mean and maximum $\delta^{13}C$ anomaly statistics.** Cores with a latitude higher than 40°S are designated as Southern Ocean.

| | ***Running Mean*** | | | | ***Maximum*** | | | |
|---|---|---|---|---|---|---|---|---|
| **Basin** | **Average (‰)** | **Stdev** | **n** | **SE** | **Average (‰)** | **Stdev** | **n** | **SE** |
| Pacific | -0.31 | 0.16 | 28 | 0.03 | -0.43 | 0.15 | 28 | 0.03 |
| Atlantic | -0.35 | 0.41 | 30 | 0.08 | -0.51 | 0.46 | 30 | 0.08 |
| Southern | -0.3 | 0.19 | 10 | 0.06 | -0.42 | 0.19 | 10 | 0.06 |
| Indian | -0.28 | 0.16 | 2 | 0.11 | -0.4 | 0.21 | 2 | 0.15 |

*i. Pacific Ocean*

The Pacific Ocean has an average maximum $\delta^{13}C$ anomaly of -0.43 ± 0.03‰ (1SE) and an average running mean $\delta^{13}C$ anomaly of -0.31 ± 0.03‰ (1SE) (Table 1). $\delta^{13}C$ records from the western tropical Pacific (WTP) and eastern equatorial Pacific (EEP) provide the opportunity to evaluate the minima between two oceanographically distinct regions of the Pacific Ocean. Specifically, utilizing the WTP and EEP records, we can compare the $\delta^{13}C$ minima in an upwelling region with thin a thermocline to those from a convergence zone with a thicker thermocline (Figure 7). Focusing on the WTP, the average maximum anomaly is -0.44 ± 0.05‰ (1SE) and the average running mean anomaly is -0.30 ± 0.05‰ (1SE) (Table 2). Maximum and running mean $\delta^{13}C$ minima in the EEP are similar to the WTP, with average values of -0.42 ± 0.04‰ (1SE) and -0.31 ± 0.04‰ (1SE), respectively (Table 2). The mean anomalies in the WTP and EEP are within one standard error of one another, indicating there is no significant difference in the mean $\delta^{13}C$ signals (Figure 7). Both regions contain a substantial number of cores for a comprehensive analysis (WTP: n = 11, EEP: n = 16) but there are more Tier 1 records in the EEP (n = 11) than the WTP (n = 3). The majority of records in the WTP are Tier 3 (n = 8), suggesting the $\delta^{13}C$ signal in this region is likely muted.

**Table 2. Western Tropical Pacific (WTP) and Eastern Equatorial Pacific (EEP) running mean and maximum $\delta^{13}C$ anomaly statistics.** Calculations for running mean and maximum $\delta^{13}C$ anomalies are as described in Table 1.

| | *Running Mean* | | | | *Maximum* | | | |
|---|---|---|---|---|---|---|---|---|
| **Region** | **Average (‰)** | **Stdev** | **n** | **SE** | **Average** | **Stdev** | **n** | **SE** |
| WTP | -0.30 | 0.17 | 11 | 0.05 | -0.44 | 0.17 | 11 | 0.05 |
| EEP | -0.31 | 0.16 | 16 | 0.04 | -0.42 | 0.14 | 16 | 0.04 |

*ii. Atlantic Ocean*

The Atlantic Ocean has an average maximum $\delta^{13}C$ anomaly of -0.51 ± 0.08‰ (1SE) and an average running mean anomaly of -0.35 ± 0.08‰ (1SE) (Table 1). The Atlantic possesses the largest range in $\delta^{13}C$ signals, with an anomaly of -2.10‰ located in the Benguela upwelling region (Schneider et al., 1992) and the smallest anomaly of 0‰ located off the Iberian Peninsula (Abrantes et al., 1998) (Figure 8). Several records in the Atlantic have periods of increasing and decreasing $\delta^{13}C$ during the deglaciation (Table A2). As none of these records are Tier 1, it is difficult to determine whether these records exhibit positive or negative anomalies during HS1.

*iii. Southern Ocean*

Cores located at latitudes higher than 40°S are influenced by upwelling of nutrient rich water from the abyss and therefore considered to be in the Southern Ocean (Figure 9). The Southern Ocean cores are all located north of the Polar Front (PF), spanning the latitude range from 40°S to 54°S. The average Southern Ocean maximum and running mean $\delta^{13}C$ anomalies are -0.42 ± 0.06‰ (1SE) and -0.30 ± 0.06‰ (1SE), respectively. These results are within one standard deviation of the $\delta^{13}C$ anomalies in other ocean basins (Table 1).

*iv. Indian Ocean*

The Indian Ocean $\delta^{13}C$ signal is characterized by the smallest number of $\delta^{13}C$ records (n = 2) of all the ocean basins (Figure 6), making it difficult to accurately assess the region. Nevertheless, the existing data yield a maximum average anomaly of -0.40 ± 0.15‰ (1SE) and an average running mean

anomaly is -0.28 ± 0.16‰ (1SE) (Table 1), similar to the results in the Atlantic, Pacific, and Southern Oceans.

c) Deglacial SST Records

*i. Sub-Polar*

Among the three temperature regions, the largest rise in SST between the LGM and HS1 occurred in sub-polar latitudes, where two records suggest that SSTs increased by ~3.5°C (Figure 10C). The North Atlantic record (51.9°N, 12.9°W) displays a 3.5 ± 2.3°C (1σ) rise in SST, while the SW Pacific record (45.5°S, 174.3°E) shows a SST rise of 3.6 ± 1.9°C (1σ) (Table 3). Note that only one temperature record represents each of these regions and therefore the error is ± 1σ, not ± 1SE. Because there is only one SST record in the North Atlantic and SW Pacific, it is difficult to assess whether these time series are representative of their respective regions. Temperature differences from the North Atlantic and SW Pacific also exhibit the largest standard deviation amongst all the regions (Table 3) which is due to the large variability within each record (Figure 10C).

**Table 3. Regional average temperature rises between the LGM and HS1.** The temperature rise for each region is calculated by subtracting averaged LGM temperatures (19-23 kyr BP) from averaged HS1 temperatures (14.5-17.5 kyr BP). In cases where more than one record exists for a region, the calculated temperature rises are averaged.

| Region | Temperature Rise (°C) | Stdev | n | SE |
|---|---|---|---|---|
| E. Pacific | 1.2 | 0.8 | 4 | 0.4 |
| W. Pacific | 1.3 | 0.8 | 5 | 0.3 |
| SW Pacific | 3.6 | 1.9 | 1 | - |
| North Atlantic | 3.5 | 2.3 | 1 | - |
| African Margin | 0.5 | 0.7 | 1 | - |
| SW Atlantic | 1.3 | 0.8 | 1 | - |
| SE Atlantic | 0.4 | 1.3 | 1 | - |
| Indian Ocean | 0.9 | 0.4 | 4 | 0.2 |

*ii. Sub-Tropical*

The spatial coverage of subtropical SST records is also limited, characterized by two time series from the southeast and southwest Atlantic (Figure 10B). The SE Atlantic record, which is located slightly south of the Benguela upwelling region (34.1°S, 17.3°E), shows an LGM to HS1 temperature rise of 0.4 ± 1.3°C (1σ). The error is more than double the temperature signal due to the noisiness of the data. The SW Atlantic record, which is at a similar latitude (32.5°S, 50.2°W), shows a larger temperature signal of 1.30 ± 0.80°C (1σ), but it has a poorly characterized LGM interval (Figure 10B). Given the limitations of the records, we assume that temperatures warmed by approximately 1°C in the South Atlantic.

*iii. Tropical*

Time series of deglacial SSTs in the tropics are more robust than either the sub-polar or sub-tropical regions because of the larger number of records available. The estimated temperature signal for the tropical records are all within one standard deviation of one another (Table 3). The average temperature signal in the WTP (1.3 ± 0.8°C, 1σ) is consistent with the average signal in the EEP (1.2 ± 0.8°C, 1σ) (Figure 10A, Table 3). Results from both regions are derived from multiple temperature records, implying the estimated SST rise for both regions is well constrained. The stacked Indian Ocean temperature record shows a small LGM to HS1 temperature rise of 0.9 ± 0.4°C (1σ) (Figure 10A). The northwest African Margin record (12.44°N, 18.04°W) presents an even smaller SST rise of 0.5 ± 0.7°C (1σ) (Figure 10A). Local oceanographic effects may bias regions with rising SSTs represented by only one temperature record. In the discussion section, we therefore place the most emphasis on the tropical records where the temperature trends are clear and replicated between multiple sites.

*iv. HS1 Time Interval*

Sea surface temperature signals vary over the course of HS1, especially in regions represented by only a few records (Figure 10). Using an average temperature spanning the entire HS1 interval may therefore not capture the full extent of the LGM to HS1 temperature signal. To assess the sensitivity of the signal to our choice of time interval, we estimated temperatures using two different time intervals:

14.5-15.5 kyr BP and 14.5-17.5 kyr BP. The results of this exercise showed slightly larger temperature changes relative to the LGM for 14.5-15.5 kyr BP compared to 14.5-17.5 kyr BP. In their respective regions the temperature signals were, however, within one standard deviation of one another, indicating the temperature signal is not strongly dependent on time interval.

d) Potential Influence of Deglacial SST Rise on $\delta^{13}C$ Anomalies

Using the thermodynamic relationship of air-sea gas exchange and the regional SST signals, we estimated the maximum SST contribution to planktonic $\delta^{13}C$ anomalies. The largest temperature-dependent $\delta^{13}C$ effect occurs in the North Atlantic (-0.35 ± 0.23‰, 1σ) and SW Pacific (-0.36 ± 0.19‰, 1σ) (Figure 11). In the sub-tropics, the temperature-dependent signals are smaller, with an air-sea effect in the SE Atlantic and SW Atlantic of -0.04 ± 0.13‰ (1σ) and -0.13 ± 0.08‰ (1σ), respectively (Figure 11). In the tropics, rising temperatures decrease surface ocean $\delta^{13}C$ by up to 0.13 ± 0.08‰ (1σ) and 0.12 ± 0.08‰ (1σ) for the WTP and EEP, respectively. Temperature-induced $\delta^{13}C$ signals are likely the smallest in the Indian Ocean (-0.09 ± 0.04‰, 1σ) and African Margin (-0.05 ± 0.07‰, 1σ). Because it takes ~10 years for ocean and atmospheric $\delta^{13}C$ to reach isotopic equilibration (Broecker and Peng, 1974), we view these temperature-dependent results as a maximum effect on the $\delta^{13}C$ anomalies.

e) Species-based $\delta^{13}C$ Minima

To investigate potential $\delta^{13}C$ signal dependence attributed to the planktonic foraminiferal species, we averaged the maximum $\delta^{13}C$ anomalies for each species. We find that in the surface mixed layer, symbiont bearing *G. sacculifer* and non-symbiont bearing *G. bulloides* have average $\delta^{13}C$ anomalies of -0.35 ± 0.03‰ (1SE) and -0.42 ± 0.05‰ (1SE), respectively. The two symbiont bearing species characterizing the thermocline, *N. dutertrei* and *G. menardii*, have average minima of -0.46 ± 0.05‰ (1SE) and -0.75 ± 0.07‰ (1SE), respectively. The non-symbiont bearing *G. inflata*, also representing thermocline $\delta^{13}C$, has an average of -0.44 ± 0.08‰ (1SE). All of the averages are calculated from the maximum anomalies, excluding two apparent outliers from a *G. bulloides* record (-2.1‰) and a *G. inflata*

record (-1.4‰) (Schneider et al., 1992) that were driving their respective averages 0.1-0.2‰ larger in magnitude. The larger magnitude of the *G. menardii* average is likely because only two records represent this species, one from the WTP and one from the EEP (Figure 7). Nevertheless, with the exception of *G. menardii*, there is a general consistency between the different species and their average $\delta^{13}C$ minima and there appears to be no signal bias dependent on algal symbionts (Figure 12).

f) New Planktonic Stable Isotope Records

Stable isotope results for GGC10 and GGC13 generated in this study are offset from the published results of Thunell et al. (1992) (here on T92) (Figure 13). Although $\delta^{18}O$ offsets of 0.3‰ are not uncommon between different laboratories (Hodell et al., 2003; Ostermann and Curry, 2000), we find mean $\delta^{18}O$ offsets of -0.58 ± 0.07‰ (1SE) and -0.93 ± 0.08‰ (1SE) for GGC10 and GGC13, respectively. $\delta^{13}C$ results have smaller mean offsets of -0.48 ± 0.02‰ (1SE) for GGC10 and -0.53 ± 0.03‰ (1SE) for GGC13. These offsets may be due to different sample preparation methods including different *G. sacculifer* size fractions (i.e. T92 used 200-250 μm and this study used 300-355 μm) (Figure 13) (Oppo and Fairbanks, 1989) and whether the foraminifera were crushed or left whole prior to acidification (Lund and Curry, 2006).

For MW91-9-15, $\delta^{18}O$ and $\delta^{13}C$ offsets between Patrick and Thunell (1997) (here on PT97) and this study are considerably smaller than the GGC10 and GGC13 results (Figure 14). The calculated mean $\delta^{18}O$ offset of -0.22 ± 0.05‰ (1SE) is similar to offsets observed in earlier studies (Hodell et al., 2003; Ostermann and Curry, 2000). The calculated mean $\delta^{13}C$ offset is negligible (0.003 ± 0.037‰, 1SE), likely because the *G. sacculifer* size fraction used for stable isotope analysis was consistent between this study and PT97 (i.e. both used 300-355 μm size fraction).

Overall, the $\delta^{18}O$ offsets are of less concern than $\delta^{13}C$ offsets because we only use $\delta^{18}O$ as a stratigraphic tool in this study, whereas we use the $\delta^{13}C$ records to calculate the sea surface anomalies. The $\delta^{13}C$ offsets are too large in GGC10 and GGC13 and therefore prevent the merging of the new and

T92 records. Instead, we use the new data to verify the anomalies determined from the T92 results, improving our overall confidence in the $\delta^{13}C$ anomalies established from these cores. Both new and T92 $\delta^{13}C$ results for GGC10 show a stable LGM from 19-23 kyr BP and a steady decrease in $\delta^{13}C$ starting at ~18 kyr BP and ending at ~15 kyr BP (Figure 13C). At 15.5 kyr BP, a one-point spike in $\delta^{13}C$ in the new GGC10 results may be the result of bioturbation (i.e. the data point at 15.5 kyr BP in both the $\delta^{13}C$ and $\delta^{18}O$ are similar to their respective LGM values). Calculating the $\delta^{13}C$ anomaly from the new $\delta^{13}C$ results yields an anomaly of -0.35‰ (±0.09‰, 1σ), which is slightly less than the T92 $\delta^{13}C$ anomaly of -0.43‰ (±0.09‰, 1σ). Thus, despite the large mean offsets between laboratories, the $\delta^{13}C$ anomalies are very similar.

There is a larger disparity between the $\delta^{13}C$ anomalies estimated from T92 and the new results for GGC13. The T92 $\delta^{13}C$ record has steady LGM values (±0.04‰, 1σ) and begins to decrease at ~19 kyr BP. The new $\delta^{13}C$ results show a slightly varied signal during the LGM (±0.14‰, 1σ), but $\delta^{13}C$ values begin to decrease at ~19 kyr BP. The T92 results reach a minimum in $\delta^{13}C$ at 16.5 kyr BP (i.e. the middle of HS1) before continuing to decrease for the remainder of the deglaciation (Figure 13D). Unlike the T92 results, the new $\delta^{13}C$ record does not continue to decrease after HS1 (Figure 13D). Calculating the maximum anomaly for the new data yields a $\delta^{13}C$ anomaly of -0.32‰ (±0.14‰, 1σ). Compared to the T92 maximum $\delta^{13}C$ anomaly of -0.68‰ (±0.04‰, 1σ), the new $\delta^{13}C$ record produces an anomaly of roughly half of T92, likely as a result of the methodology.

As mentioned in the methods section, the minimum $\delta^{13}C$ value used to calculate the anomalies are selected between the ages of 12 to 18 kyr BP. The T92 $\delta^{13}C$ results show $\delta^{13}C$ continuing to decrease after HS1, reaching ~0.7‰ at 12 kyr BP, which is the deglacial data point used to calculate the maximum anomaly of 0.68‰. The new $\delta^{13}C$ record reaches its minimum deglacial value at ~18 kyr BP, however (Figure 13D). If we calculate the T92 anomaly specifically using the HS1 interval (14.5-17.5 kyr BP), it becomes -0.29‰ (±0.04‰, 1σ), a value much more comparable to the -0.32‰ anomaly estimated from the new data. Because the patterns between the T92 and new $\delta^{13}C$ records are comparable from the LGM

to HS1 and then diverge (Figure 13D), we are more confident in the T92 $\delta^{13}C$ anomaly calculated from the 14.5-17.5 kyr BP time interval. Thus, the choice of time window, at least in this case, impacts the overall magnitude of the $\delta^{13}C$ signal.

The new $\delta^{13}C$ results for MW91-9-15 reveal a larger $\delta^{13}C$ anomaly than the PT97 results, with a new maximum $\delta^{13}C$ anomaly of -0.46‰ (±0.11‰, 1σ), compared to the $\delta^{13}C$ anomaly of -0.23‰ (±0.08‰, 1σ) from PT97. A new running mean anomaly of -0.23‰ (±0.11‰, 1σ) is also more negative than the PT97 running mean anomaly of -0.09‰ (±0.08‰, 1σ). In the new $\delta^{13}C$ record, multiple data points outline a continuous decrease in $\delta^{13}C$ during HS1, allowing us to better identify the anomaly (Figure 14B). Because the $\delta^{13}C$ signal in the PT97 record is characterized by only one data point, the anomaly poorly characterized. Compiling the two records results in a maximum anomaly of -0.40‰ (±0.10‰, 1σ) and a running mean anomaly of -0.22‰ (±0.10‰, 1σ). Thus, with the improved resolution, MW91-9-15 has a more robust sampling size and therefore better captures the $\delta^{13}C$ signal.

**4. Discussion**

The aim of this thesis project is to evaluate the biological pump and Southern Ocean hypotheses by assessing spatial patterns in the surface ocean $\delta^{13}C$ minima. We assess $\delta^{13}C$ anomalies in the four main ocean basins: Atlantic, Pacific, Indian, and Southern Oceans, and in sub-regions including the North Atlantic, South Atlantic, eastern equatorial Pacific (EEP), and western tropical Pacific (WTP). Each region is evaluated against the SL15 modeling results (Schmittner and Lund, 2015). In addition, we use the EEP and WTP to compare the $\delta^{13}C$ minima between an upwelling region and a convergence zone. Surface water $\delta^{13}C$ anomalies of similar magnitude in multiple locations would support a biological pump mechanism. Smaller anomalies in upwelling areas influenced by mode and intermediate waters would also be consistent with the biological pump hypothesis. Larger $\delta^{13}C$ anomalies in the Southern Ocean and other upwelling regions would support enhanced ventilation of a $^{13}C$-depleted abyssal water mass at the onset of the last deglaciation, thus supporting the Southern Ocean hypothesis.

Following the spatial analysis, additional discussion points are addressed. We account for the effects of air-sea gas exchange caused by rising deglacial SST on the surface ocean $\delta^{13}C$ minima and briefly discuss $\delta^{13}C$ signal dependence based on the planktonic foraminiferal species type. We also discuss the stable isotope records from the WTP: GGC10, GGC13, and MW91-9-15. The new planktonic $\delta^{18}O$ and $\delta^{13}C$ records are compared to the original records from T92 (Thunell et al., 1992) and PT97 (Patrick and Thunell, 1997). $\delta^{18}O$ and $\delta^{13}C$ offsets between the newly generated and the original records are evaluated and potential causes are discussed. We then address the implications of data showing positive $\delta^{13}C$ anomalies found at intermediate depths (~1 km) during HS1 and compare them to the SL15 model results. Finally, we conclude the discussion by outlining the future research necessary to assess the ultimate cause of the carbon isotope minima at the onset of the last deglaciation.

a) Global Surface Ocean $\delta^{13}C$ Anomaly

The SL15 model results show a ~0.3‰ decrease in global sea surface $\delta^{13}C$ due to the AMOC-triggered weakening of the biological pump. By comparison, the average maximum Tier 1 and Tier 2 results show a ~0.5‰ decrease. The most likely explanation for the ~0.2‰ discrepancy is the influence of rising deglacial SSTs on air-sea gas exchange. In SL15, there is minimal change in mean surface ocean temperature, so weakening of the biological pump is the main driver of surface ocean $\delta^{13}C$ signal. By comparison, temperature reconstructions suggest that SSTs rose by ~2°C on average from the LGM to HS1 (Shakun et al., 2012). The estimated temperature rise from our compilation, however, only shows an average rise in temperature of ~1°C (Figure 11). The Shakun et al. (2102) compilation may better capture the larger temperature signal in higher latitude regions, resulting in a larger estimated temperature rise. Air-sea gas exchange therefore could have increased the magnitude of the observed sea surface $\delta^{13}C$ anomalies by 0.1-0.2‰, assuming complete equilibration (thermodynamic slope = -0.1‰ / °C). Accounting for temperature-dependent air-sea gas exchange reduces the global $\delta^{13}C$ anomaly from -0.5‰ to -0.3‰ or -0.4‰, which is closer to the SL15 modeled global average. Thus, air-sea gas exchange may account for the discrepancy between modeled and observed $\delta^{13}C$ anomalies, suggesting that the observed

oceanic and atmospheric $\delta^{13}C$ anomalies are due to a combination of biological pump and temperature effects. It is unlikely that temperature is fully responsible for the discrepancy, however, because we would observe a positive anomaly in $\delta^{13}C$ of the atmosphere upon reaching isotopic equilibrium, opposite of observations (Figure 1B). Broad swaths of the Southern Ocean show positive or near zero anomalies as an outcome of the SL15 model (Figure 4), which are likely also contributing to the 0.2‰ discrepancy along with rising SSTs.

b) Basin-scale Surface Ocean $\delta^{13}C$ Minima

The consistency of $\delta^{13}C$ anomalies between ocean basins also favors a biological pump mechanism. Ranging from -0.4‰ to -0.5‰, the average maximum $\delta^{13}C$ anomalies are within 1SE of one another (Table 1). Likewise, the slightly smaller running mean anomalies (~ -0.3‰) are also within 1SE of one another (Table 1). The spatial pattern of decreasing surface ocean $\delta^{13}C$ is generally consistent between the paleo-records and the SL15 modeling results. In the SL15 simulation, a weakened biological pump decreases the overall surface ocean $\delta^{13}C$ by 0.2‰ to 0.5‰ in the Pacific, Indian, South Atlantic, and Southern Oceans (Figure 4). The maximum average $\delta^{13}C$ anomalies of -0.43 ± 0.03‰ (1SE), -0.40 ± 0.15‰ (1SE), and -0.42 ± 0.06‰ (1SE) for the Pacific, Indian, and Southern oceans, respectively, fall within the range of the minima from the modeling results. The observed South Atlantic $\delta^{13}C$ anomalies of -0.74 ± 0.19‰ (1σ) are higher than the modeling results, most likely driven by the large $\delta^{13}C$ minima in the Benguela upwelling region (Figure 8). Simulated positive $\delta^{13}C$ anomalies in the North Atlantic and south of 60°S in the Southern Ocean (Figure 4) will be discussed in further detail below.

*i. North Atlantic*

The simulated $\delta^{13}C$ signal in the North Atlantic is highly variable, with some regions showing negative anomalies and other regions positive values (Figure 4). The complexity is due to the direct and indirect effects of a weakened AMOC. Positive $\delta^{13}C$ anomalies are due to reduced sinking of high $\delta^{13}C$ surface water while negative anomalies are driven by a weakened biological pump. The spatial

heterogeneity of the North Atlantic $\delta^{13}C$ signal make it a non-ideal region to evaluate the biological pump hypothesis. Additionally, the region is completely lacking in high-quality Tier 1 data (Figure 8). Our discussion therefore focuses on the Southern, Pacific, South Atlantic, and Indian ocean basins where modeling results suggest the effect of the biological pump will be the most apparent (Schmittner and Lund, 2015).

*ii. Southern Ocean*

The Southern Ocean hypothesis is based on the premise that enhanced upwelling transported isotopically light carbon from the abyss to the surface of the Southern Ocean, which was then advected to lower latitudes via AAIW and SAMW (Spero and Lea, 2002). Because the light carbon would make first contact with surface waters in the Southern Ocean, the minima should be largest in this region. The uniformity between the carbon isotope minima in the Southern Ocean and the other ocean basins is inconsistent with a southern origin, however. Instead, the spatial averages suggest that Southern Ocean $\delta^{13}C$ minima are similar to other ocean basins (Table 1). An important caveat is that most of the constraints are from north of the Sub-Antarctic Front (SAF) and are therefore north of the region where deep upwelling occurs (i.e. south of the Polar Front) (Figure 9). Nevertheless, deep upwelling results in high nutrient concentrations throughout the Southern Ocean, so we would expect to see some sign of unusually large $\delta^{13}C$ anomalies, even at the latitudes of the available cores (40°S to 54°S). Thus, the similar $\delta^{13}C$ signal in the Southern Ocean and the other basins is more consistent with the biological pump hypothesis than the Southern Ocean hypothesis.

Despite the limited data coverage in the Southern Ocean, we can use the available records to assess spatial gradients and their consistency with each hypothesis. Because deep waters upwell south of the of the Polar Front, $\delta^{13}C$ anomalies should be largest in this region and then become progressively smaller as the $\delta^{13}C$ signal becomes altered by air-sea gas exchange or mixing with high $\delta^{13}C$ surface waters at lower latitudes. With the exception of the large Tier 3 anomaly at ~45°S (-0.74 ± 0.19‰, 1σ), the Southern Ocean data show a general trend of increasing $\delta^{13}C$ anomalies with decreasing latitude

(Figure 15). A similar relationship emerges when plotting the Southern Ocean minima against the location of the subtropical Front (STF), with the generally larger $\delta^{13}C$ anomalies north of the STF and smaller anomalies south of the front (Figure 16). This pattern is the opposite of what we would predict if the low $\delta^{13}C$ signal was advected northward from ~60ºS and is therefore inconsistent with the Southern Ocean hypothesis.

The pattern of increasing $\delta^{13}C$ minima with decreasing latitude in the Southern Ocean is in agreement with the biological pump hypothesis. In the SL15 modeling results, positive surface ocean $\delta^{13}C$ anomalies south of ~60°S result from the upwelling of anomalously heavy carbon from intermediate depths. Positive $\delta^{13}C$ anomalies at intermediate depths are the outcome of reduced export of isotopically light organic carbon from the low latitude surface ocean. Upwelling of intermediate-depth water in the Southern Ocean therefore causes higher surface ocean $\delta^{13}C$ values, resulting in positive $\delta^{13}C$ anomalies south of 60°S (Figure 4). North of 60°S, the anomalies reverse sign and become progressively more negative until reaching a plateau of -0.4‰ at approximately 40°S (Figure 4). Our compilation shows a similar pattern, with the most negative anomalies generally occurring north of 45°S (Figure 15). The primary exception to the trend is the core at 45°S (in the Indian sector of the Southern Ocean) where the $\delta^{13}C$ anomaly is large relative to results from the same latitude range (Figure 15). Given the low quality of this record (a Tier 3 time series with average sampling resolution of 3 kyr) and the general paucity of data from the Southern Ocean, it is unclear whether this result is a one-point outlier or it is indicative of a very large $\delta^{13}C$ signal in this region. Temperature is unlikely to explain the $\delta^{13}C$ trend because the largest deglacial SST rise occurred at 45°S and the smallest at 34°S (Table A3), the opposite requirement to account for the latitudinal trend. Taking all of the available data into consideration, it appears that the meridional trend in $\delta^{13}C$ anomalies is consistent with the biological pump hypothesis.

*iii. Tropical Pacific*

The eastern equatorial Pacific (EEP) and western tropical Pacific (WTP) are useful locations to reconstruct $\delta^{13}C$ signals because the EEP is an upwelling-dominated regime while the WTP is primarily

characterized by Ekman convergence. The large number of cores in each region, including many Tier 1 records, means the $\delta^{13}C$ minima in these locations are well characterized. WTP and EEP average maximum $\delta^{13}C$ anomalies, as well as the average running mean anomalies, are within 1SE of one another (Table 2), implying the carbon isotope minima are uniform across the tropical Pacific. This is a surprising result given that the EEP is dominantly an upwelling regime with cold SSTs and a thin thermocline, while the WTP is a convergence zone with a thick thermocline and high SSTs. According to the Southern Ocean hypothesis, the $\delta^{13}C$ anomalies should be larger in regions where upwelling of intermediate and mode waters occurs, like the EEP (Spero and Lea, 2002). The homogenous $\delta^{13}C$ signals between these different oceanographic regimes therefore appear to be inconsistent with the Southern Ocean hypothesis.

Multiple temperature records characterize deglacial SSTs in both the WTP (n = 5) and EEP (n = 4). From the LGM to HS1, SST increased ~1°C in both the WTP and EEP (Figure 10A, Table 3), suggesting rising temperatures contributed a maximum of ~ -0.1‰ to the $\delta^{13}C$ anomalies (Figure 11). Accounting for the effect of air-sea gas exchange results in $\delta^{13}C$ minima of -0.3‰ in both the WTP and EEP. Given the consistent temperature signals, SSTs cannot be invoked to explain the lack of larger $\delta^{13}C$ minima in the EEP.

In contrast to the Southern Ocean hypothesis, one of the predications of the biological pump hypothesis is that sea surface $\delta^{13}C$ anomalies in the EEP should be smaller than in the WTP. This is because intermediate and mode water depths in the SL15 simulations display positive $\delta^{13}C$ anomalies in response to reduced export of light carbon from the surface ocean (Figure 4). As a result, the surface ocean $\delta^{13}C$ signal in the EEP is muted by mixing with relatively high $\delta^{13}C$ water upwelled from below. Simulated $\delta^{13}C$ anomalies in the EEP average -0.2‰, compared to anomalies of -0.3‰ to -0.6‰ in the WTP (Schmittner and Lund, 2015). As previously noted, there is not a significant difference in the observed $\delta^{13}C$ minima between the EEP and WTP, which is at odds with the model results. However, the magnitude of the $\delta^{13}C$ minima in the WTP may be artificially low due to the prevalence of low resolution

records in this region. Of the 11 total records in the WTP, eight are Tier 3 and three are Tier 1. In the EEP, which has 16 total records, eleven are Tier 1 and five are Tier 2. On average, we find that Tier 3 records yield $\delta^{13}C$ anomalies that are 0.2-0.3‰ smaller than Tier 1 results (Figure 5). If we take this bias into account, the WTP signal would be 0.2-0.3‰ larger than in the EEP. Thus, the lack of contrast between the WTP and EEP signals may be due to an inherent bias in the quality of time series from the WTP. Averaging only the Tier 1 records for both the EEP and WTP results in $\delta^{13}C$ anomalies of -0.41 ± 0.05‰ (1SE, n = 11) and -0.49 ± 0.1‰ (1SE, n = 4), respectively. Although the average Tier 1 anomaly is slightly larger in the WTP, the averages are still within 1SE of one another. At this stage, we are limited to pointing out that correcting the bias in WTP records would tend to make zonal gradient in anomalies consistent with the pattern expected from the biological pump hypothesis.

*iv. South Atlantic*

The average anomaly in the South Atlantic is larger than simulated in SL15. The compiled $\delta^{13}C$ records have an average maximum anomaly of -0.74 ± 0.19‰ (1SE) and an average running mean anomaly of -0.55 ± 0.18‰ (1SE), while the model results only show a decrease of 0.2‰ to 0.5‰ in surface ocean $\delta^{13}C$. The larger average from the $\delta^{13}C$ records is driven by one sediment core (GEOB1023-5) that has two very large $\delta^{13}C$ anomalies, one from a *G. bulloides* record (-2.1‰) and the other from a *G. inflata* record (-1.4‰) (Figure 8) (Schneider et al., 1992). Because GEOB1023-5 is located in the Benguela upwelling region these records appear to be consistent with the Southern Ocean hypothesis prediction of larger $\delta^{13}C$ anomalies in upwelling regimes. The one available temperature record from the SE Atlantic shows a SST rise of 0.4°C (Figure 10B, Table 3), implying temperature dependent air-sea gas exchange would only account for -0.04‰ of these larger minima. The SE Atlantic temperature record (34.1°S, 17.34°E) is ~4° south of the southern edge of the Benguela upwelling regime (Figure 8), however, indicating that this record is not appropriate for gauging SSTs further north. Given that the GEOB1023-5 $\delta^{13}C$ anomalies are far larger than any other documented signal in the published literature, we speculate they may reflect locally enhanced upwelling of light carbon during HS1, rather

than a significant change in endmember $\delta^{13}C$ emanating from the Southern Ocean. Indeed, a nearby core located near the center of the Benguela upwelling region has a smaller $\delta^{13}C$ anomaly of -0.6‰ (V19-258) (Figure 8). Thus, the two larger minima from GEOB1023-5 are outliers that are potentially recording other influences on surface water $\delta^{13}C$ in that area. Excluding the two large $\delta^{13}C$ anomalies from GEOB1023-5, the maximum and running mean average $\delta^{13}C$ minima in the South Atlantic become -0.49 ± 0.08‰ (1SE) and -0.30 ± 0.07‰ (1SE), respectively, and are more comparable to the SL15 results.

*v. Indian Ocean*

The Indian Ocean represents the smallest average $\delta^{13}C$ minima of all the regions, with a maximum of -0.40 ± 0.15‰ (1SE) and a running mean of -0.28 ± 0.16‰ (1SE). The smaller averages and large standard errors are due to the lack of $\delta^{13}C$ records from the Indian Ocean (n = 2) (Figure 6, Table 1). Four temperature records depict the SST rise in the Indian Ocean, however (Table 3). The estimated deglacial SST rise for the Indian Ocean is ~1°C (Figure 10A, Table 3), indicating increasing temperatures can account for up to -0.1‰ of the $\delta^{13}C$ signal in the region (Figure 11). Because two of the Mg/Ca records are generated from the same core as one of the $\delta^{13}C$ records (WIND28K; Table A3 and A7), -0.1‰ is a reasonable estimate for this location. Nevertheless, it is clear that rising SSTs cannot account for the full $\delta^{13}C$ signal in the Indian Ocean.

c) <u>Rising Deglacial SSTs</u>

Although increasing surface temperatures yield lower surface ocean $\delta^{13}C$ through air-sea gas exchange, rising SSTs cannot account for the full magnitude of the $\delta^{13}C$ minima. The residence time of a water mass in the surface ocean is generally less than that required to reach isotopic equilibrium (~10 years) (Broecker and Peng, 1974; Broecker and Maier-Reimer, 1992). Our regional temperature results should therefore be considered a maximum effect of air-sea gas exchange on the $\delta^{13}C$ anomalies. Given the typical LGM to HS1 SST change of ~1°C (Table 3) the temperature effect would be approximately -0.1‰ in well equilibrated regions (thermodynamic slope = -0.1‰ / °C) (Figure 11). As the average

maximum anomaly in each region is -0.4‰ or larger (Table 1), rising SST cannot be responsible for the full surface ocean $\delta^{13}C$ signal. Furthermore, if increasing temperatures were the sole driver of the surface ocean $\delta^{13}C$ anomalies, we would see a positive $\delta^{13}C$ anomaly in the atmosphere during HS1 resulting from the isotopic equilibration between oceanic and atmospheric $\delta^{13}C$, which is opposite the pattern observed in ice cores (Figure 1B). Thus, temperature likely plays a role in the $\delta^{13}C$ signals, but it is secondary to other effects.

d) Species-based $\delta^{13}C$ Minima

Averaging the maximum $\delta^{13}C$ anomalies for each planktonic foraminiferal species allows us to investigate potential signal dependence based on the species used for carbon isotope analysis. For the surface mixed layer symbiont bearing *G. sacculifer* and non-symbiont bearing *G. bulloides* have average $\delta^{13}C$ anomalies of -0.35 ± 0.03‰ (1SE) and -0.42 ± 0.05‰ (1SE), respectively. The two symbiont bearing species characterizing the thermocline, *N. dutertrei* and *G. menardii*, have average minima of -0.46 ± 0.05‰ (1SE) and -0.75 ± 0.07‰ (1SE), respectively. The non-symbiont bearing *G. inflata*, also representing thermocline $\delta^{13}C$, has an average of -0.44 ± 0.08‰ (1SE). Overall, there is a general consistency between the different species and their average $\delta^{13}C$ minima with the exception of *G. menardii*, which has an average anomaly of ~0.3‰ larger than the other species (Figure 12). Because *G. menardii* is represented by only two records, one located in the WTP, a convergence zone, and the other in the EEP upwelling regime (Figure 7), it is unlikely the large anomalies are due to the character of the oceanographic location. Both *G. menardii* anomalies are accompanied by smaller *G. sacculifer* anomalies estimated from the same respective cores (Figure 7), implying those specific locations are not characterized by larger minima, leading us to believe the larger *G. menardii* anomaly is due to the lack of records or an issue with the species ability to accurately record $\delta^{13}C$ of DIC. There appears to be no signal bias in whether or not a species possesses algal symbionts (Figure 12). With the exception of *G. menardii,* we find no signal dependence based on the planktonic foraminiferal species used in this $\delta^{13}C$

compilation, suggesting that vital effects are not a primary control on $\delta^{13}C$ anomalies during the last deglaciation.

e) New Planktonic Stable Isotope Records

*i. $\delta^{13}C$ and $\delta^{18}O$ Offsets*

Planktonic $\delta^{13}C$ results in the western tropical Pacific (WTP) highlight the need to use a consistent size fraction when conducting stable isotope analyses on foraminifera. To review, in core GGC10, the mean $\delta^{13}C$ offset between 200-250 μm (T92) and 300-355 μm (this work) size fractions of *G. sacculifer* is -0.48‰ (Figure 13C). Similarly, GGC13 has an offset of -0.53‰ (Figure 13D). Oppo and Fairbanks (1989) found that *G. sacculifer* $\delta^{13}C$ increases with increasing shell size, with offsets in $\delta^{13}C$ of up to ~0.5‰ amongst neighboring 50 μm-increment size fractions. The magnitude of the $\delta^{13}C$ offsets is comparable to those in GGC10 and GGC13, suggesting that size fraction is the primary factor controlling mean offsets in $\delta^{13}C$ for these cores. The size-$\delta^{13}C$ relationship is likely due to growth under different light levels resulting from changes in the symbiont photosynthetic rate (Spero and Lea, 1993), suggesting that larger *G. sacculifer* are enriched in $^{13}C$ and grow in a shallower, high light environment. High light conditions would increase the symbiont photosynthetic rate, rendering the water immediately surrounding the foraminifera depleted in $^{12}C$, therefore increasing the $\delta^{13}C$ of DIC used to secrete calcite (Spero and Lea, 1993). Applying this logic to our results suggests the 300-355 μm *G. sacculifer* had a shallower depth habitat than the 200-250 μm size fraction.

We can also use the $\delta^{18}O$ results to assess whether the different size fractions of G. sacculifer secrete calcite at different water depths. The mean $\delta^{18}O$ offsets between the 200-250 μm and 300-355 μm size fractions are -0.6‰ and -0.9‰ for GGC10 and GGC13, respectively (Figure 13A, B). $\delta^{18}O_{calcite}$ generally increases with depth due to decreasing temperature and increasing salinity (Spero et al., 2003). We constructed a depth profile of $\delta^{18}O_{calcite}$ using local estimates of $\delta^{18}O_{seawater}$ and temperature, where the $\delta^{18}O_{seawater}$ was determined using modern salinity and $\delta^{18}O_{seawater}$ data from 0-100 m in the WTP (23°S-

23°N, 110°E-170°W) (Schmidt et al., 1999). A vertical temperature profile near the GGC10 and GGC13 core sites (World Ocean Atlas 2001, 11.5°N, 118.5°E) and the *G. sacculifer* paleothermometry equation from Spero et al. (2003) was then used to estimate $\delta^{18}O_{calcite}$ (Figure 17). We estimate that $\delta^{18}O_{calcite}$ ranges from -2.8‰ at 30 m to -1.5‰ at 100 m, which spans the depth range over which *G. sacculifer* calcifies (30-80 m) (Sagawa et al., 2012). Because our $\delta^{13}C$ results imply a shallower depth habitat for the larger size fraction, we expect $\delta^{18}O$ to be more negative for the 300-355 μm than the 200-250 μm size fraction. However, our results show the opposite (Figure 13A, B), suggesting the mean $\delta^{18}O$ offsets are not due to depth habitat. This may in part be an artifact of using modern values for the salinity, $\delta^{18}O_{water}$, and temperature profiles. Using modern data may have led us to believe *G. sacculifer* calcified in the $\delta^{18}O_{calcite}$ gradient, when it is possible that during HS1 and the LGM the $\delta^{18}O_{calcite}$ gradient deepened, leaving *G. sacculifer* to calcify in waters where the $\delta^{18}O_{calcite}$ is constant with depth. Therefore, the observed $\delta^{18}O$ offsets are unlikely due to depth habitat, but likely result from other problems.

The $\delta^{18}O$ offsets the two between *G. sacculifer* size fractions may be driven by a combination of issues. Elderfield et al. (2002) found a slight increase in *G. sacculifer* $\delta^{18}O$ (~0.2‰) between the 212-250 μm and 300-355 μm size fractions. However, the difference in $\delta^{18}O$ between size fractions cannot account for the full $\delta^{18}O$ offsets found in GGC10 and GGC13. In combination with the $\delta^{18}O$ offsets that are frequently observed between laboratories (~0.3‰) (Hodell et al., 2003; Ostermann and Curry, 2000), it may be possible to account for the difference in mean $\delta^{18}O$ values for GGC10 (~ -0.6‰). The larger mean $\delta^{18}O$ offset of ~0.9‰ in GGC13 appears to be driven by a one-point outlier in the T92 record at 27 kyr BP (Figure 13B). The corresponding data point in the $\delta^{13}C$ record (Figure 13D) suggests it was likely due to bioturbation. After removing the outlier from the $\delta^{18}O$ record, the new mean offset is 0.77 ± 0.06‰ (1SE), which still appears to be too large to account for with size fraction and/or laboratory-based uncertainties. Isolating the ultimate reason for the differences would require running the same size fraction of the same species in different laboratories. Given that we use the *relative* change in $\delta^{18}O$ through time to construct the isotope stratigraphy and age models for each core, such an exercise is not

essential for this project. Nevertheless, the finding of large $\delta^{18}O$ differences between labs is relevant for studies that use $\delta^{18}O$ as a water mass tracer (e.g. Lund et al., 2011; Adkins, 2013) and should be resolved to facilitate integration of $\delta^{18}O$ data from multiple labs.

Although the $\delta^{13}C$ offsets between the published and new results preclude us from combining the records into a single time series, the overall pattern within each dataset helps bolster our confidence in compiling $\delta^{13}C$ anomalies (Figure 13). The GGC10 results show similar maximum $\delta^{13}C$ anomalies for the 200-250 μm and 300-355 μm size fractions of -0.43 ± 0.09‰ (1σ) and -0.35 ± 0.09‰ (1σ), respectively. However, for GGC13, the 200-250 μm anomaly (-0.68 ± 0.04‰, 1σ) is double that for 300-355 μm (-0.32 ± 0.14‰, 1σ), suggesting that the magnitude of the $\delta^{13}C$ anomaly is entirely due to size fraction. As previously discussed in the results section, using a smaller deglacial window of 14.5-17.5 kyr BP (i.e. the HS1 time period) instead of 12-18 kyr BP, the maximum 200-250 μm anomaly becomes -0.29 ± 0.04‰ (1σ), which is within 1SE of the 300-355 μm anomaly of -0.32 ± 0.14‰ (1σ). By using a narrower time window, the large decrease in $\delta^{13}C$ after HS1 for the 200-250 μm size fraction is excluded, bringing the results into better agreement. This result suggests that deglacial anomalies in general may be sensitive to the choice of time window, which we will address in the next section. Our results suggest that regardless of mean offsets between size fractions, the magnitude of anomalies is generally very similar, consistent with earlier work showing that planktonic $\delta^{13}C$ records yield similar overall stratigraphies regardless of size fraction (Oppo and Fairbanks, 1989). Thus, compiling anomalies from various $\delta^{13}C$ records should yield reliable estimates of the overall change in surface ocean $\delta^{13}C$ of DIC during the deglaciation.

*ii. MW91-9-15*

In addition to cores GGC10 and GGC13, we re-sampled core MW91-9-15 from the western tropical Pacific (WTP) to improve its overall temporal resolution to > 1 sample per kyr. In doing so, the core moved from the Tier 3 to Tier 1 category because it already had radiocarbon dates. Unlike cores GGC10 and GGC13, however, we used the same size fraction so the results can be more easily integrated.

Combining the two records increases the sampling resolution to 1.2 samples per kyr, resulting in a new maximum anomaly of -0.40‰, which is double that of the original from PT97 (-0.23‰) (Patrick and Thunell, 1997). The MW91-9-15 $\delta^{13}C$ results are consistent with the general pattern that Tier 3 $\delta^{13}C$ anomalies are typically ~0.2‰ less than Tier 1 anomalies (Figure 5), reinforcing the notion that the WTP mean $\delta^{13}C$ anomaly is potentially muted due to the dominance of Tier 3 records in this region. Enhancing the sampling resolution of Tier 3 records should be a priority for future studies to ensure that the full amplitude of $\delta^{13}C$ anomalies is captured.

f) Influence of Deglacial Time Window

The $\delta^{13}C$ results for GGC13 demonstrate that the choice of time frame can influence the magnitude of $\delta^{13}C$ anomalies, at least for an individual core. To reiterate, using a smaller deglacial timeframe for GGC13, the $\delta^{13}C$ anomaly for the 200-250 μm size fraction was reduced by a factor of two, bringing it into reasonable agreement with the 300-355 μm results. We find the GGC13 results to be an exception rather than a rule, however. Recalculating Tier 1 and 2 $\delta^{13}C$ minima using a 14-18 kyr BP interval, we find virtually no difference in the mean anomalies between the smaller and larger time periods for both tiers. Tier 1 minima calculated from the HS1 time interval (14-18 kyr BP) are identical to the 12-18 kyr BP anomalies with averages of -0.58 ± 0.10‰ (1SE) and -0.47 ± 0.09‰ (1SE) for the maximum and running mean, respectively (Figure 5). Thus, differences in the average Tier 1 $\delta^{13}C$ anomalies between the two time intervals are negligible. Tier 2 maximum and running mean anomalies are 0.06‰ and 0.03‰ smaller using 14-18 kyr BP period, respectively, but are within 1SE of the values calculated from the 12-18 kyr BP time frame. These results suggest that the GGC13 record is anomalous and will have a minimal influence on our overall results so long as it is averaged with results from multiple cores from the same region, as we do here.

g) Intermediate Depth, Positive $\delta^{13}C$ Anomalies

Several locations display positive $\delta^{13}C$ anomalies at intermediate depths (~1 km) during HS1, in addition to negative anomalies in the surface ocean (Hertzberg et al., submitted). As with the surface ocean anomalies, the results at intermediate depths are generally consistent with the SL15 simulation (Figure 4). The net effect of the opposing trends in the surface ocean and intermediate depth records is a reduced upper ocean vertical $\delta^{13}C$ gradient (Figure 18). Such a pattern makes sense because weakening of the biological pump decreases organic carbon export from the surface ocean, driving negative anomalies in the surface ocean and positive anomalies at intermediate depths.

Isotopic results from the Brazil Margin provide a clear example of convergence between $\delta^{13}C$ in surface and intermediate waters. During the LGM, the vertical gradient ($\Delta\delta^{13}C$), or the difference between planktonic and benthic $\delta^{13}C$ records, at the Brazil Margin was ~1.3‰ (Figure 18A). $\Delta\delta^{13}C$ decreased to ~0.4‰ during HS1, reflecting an overall 0.9‰ reduction in the vertical gradient (Figure 18A). $\delta^{13}C$ records from the SW Pacific (Bostock et al., 2004) and the Southern Ocean (Pahnke and Zahn, 2005) are consistent with the Brazil Margin showing a 0.9‰ decrease in $\Delta\delta^{13}C$ during HS1 (Figure 18). In the EEP a smaller reduction in the vertical gradient of 0.6‰ is likely due to the cores location in an upwelling regime (Hertzberg et al., submitted). The decrease in $\Delta\delta^{13}C$ at multiple locations is consistent with the modeling results from SL15, which show reductions in the vertical gradient of 0.6‰ to 0.8‰ (Figure 4). The decline in the vertical gradient during HS1, shown by observations and model results, is consistent with reduced productivity and export production, thus supporting the biological pump hypothesis. It is also important to note that positive $\delta^{13}C$ anomalies at multiple intermediate depth sites are inconsistent with the Southern Ocean hypothesis. The benthic $\delta^{13}C$ records, which monitor changes in AAIW, increased by ~0.4‰ at each site during HS1 (Figure 18) (Hertzberg et al., submitted). This pattern is the opposite of what we would expect if the light isotopic signal originated from the Southern Ocean and was then advected to lower latitudes via mode and intermediate waters.

h) <u>Key Next Steps</u>

*i. Increasing Tier 3 Resolution*

In order to fully capture the deglacial $\delta^{13}C$ anomaly, it is necessary to increase the Tier 3 sampling resolution to > 1 data point per kyr. A key result of this study is that the Tier 3 anomalies are generally 0.2‰ smaller than the Tier 1 and Tier 2 anomalies, indicating that time series resolution is a primary control on estimating signal magnitude. Additionally, by enhancing the resolution of MW91-9-15, we showed that the anomaly increased by ~0.2‰, similar to pattern in the broader data compilation. As such, Tier 3 anomalies are likely misleading and should each be viewed as a minimum $\delta^{13}C$ signal. As it is unlikely we can enhance the resolution of all Tier 3 records, future work should focus on the western tropical Pacific (WTP) because of the large number of Tier 3 records located in the region. Additionally, the WTP is an area of importance for differentiating between the biological pump and Southern Ocean hypotheses. As revealed by the $\delta^{13}C$ offsets in the GGC10 and GGC13 results, the size fraction of the original $\delta^{13}C$ records should be used when increasing the resolution of Tier 3 records.

*ii. Enhancing Age Models with Radiocarbon Dates*

In order to better assess the $\delta^{13}C$ minima, all records should have age models based on radiocarbon dates to definitively define HS1 in each record. The more Tier 1 records established, the more confident we will be in the timing and magnitude of each anomaly, allowing a more accurate assessment of the carbon isotope minima, and thus the ultimate driver of rising atmospheric $CO_2$ on glacial terminations.

*iii. Southern Ocean $\delta^{13}C$ Meridional Transect*

Acquiring additional $\delta^{13}C$ records from locations south of 60°S would allow us to determine whether positive $\delta^{13}C$ minima occurred at the higher latitudes in the Southern Ocean. Specifically, evaluating a meridional transect from 40°S to 65°S would provide insight on whether the observed minima are consistent with the SL15 simulation. According to the SL15 model results, $\delta^{13}C$ anomalies become progressively smaller from ~40°S to ~50°S and then become positive south of approximately

60°S (Figure 4). A detailed meridional transect from 40°S to 65°S would therefore provide an opportunity to more definitively test the model predictions.

*iv. A More Robust Compilation of Temperature Records*

In order to conduct a full analysis on the effect of deglacial SST rise on the $\delta^{13}C$ minima, a more robust compilation of high quality temperature records is required. Currently, the temperature records are too sparse to accurately capture regional SST rises in regions other than the western tropical Pacific and eastern equatorial Pacific. Temperature records from the South Atlantic, North Atlantic, and in the Southern Ocean would be of particular interest, as those areas generally lack a desirable number of records for a comprehensive analysis. Another option would be to preform Mg/Ca-SST analyses on the same cores as the $\delta^{13}C$ records as a more precise indicator of the effect of air-sea gas exchange on surface ocean $\delta^{13}C$. This second option would allow us to directly observe the maximum contribution rising SST had on each $\delta^{13}C$ anomaly during HS1.

## 5. Conclusion

The results presented in this thesis include a global compilation of 70 planktonic $\delta^{13}C$ records and new stable isotope records for three records from the western tropical Pacific (WTP). The global Tier 1 stack shows a clear decrease in surface ocean $\delta^{13}C$ of ~0.5‰. We find a general consistency in the average $\delta^{13}C$ minima for each ocean basin for both maximum and running mean anomalies. Additionally, our results suggest that rising temperatures during the deglaciation cannot account for the full magnitude of the minima in each basin. The average $\delta^{13}C$ anomalies for the WTP and eastern equatorial Pacific (EEP) are similar and rising SST does not change the relative minima between the two regions. By categorizing the $\delta^{13}C$ records into tiers, we find that Tier 1 and Tier 2 $\delta^{13}C$ minima are ~0.2‰ larger than Tier 3 anomalies, illustrating the need to increase the resolution of the Tier 3 $\delta^{13}C$ records. The $\delta^{13}C$ offsets found between the 200-250 μm and 300-355 μm size fractions of *G. sacculifer* for GGC10 and GGC13 illuminate the issues with using different size fractions when analyzing carbon isotopes in

foraminifera. Nevertheless, the consistency in the magnitude of $\delta^{13}C$ minima calculated from the two size fractions bolsters our confidence in compiling anomalies from various sources. Increasing the sampling resolution for MW91-9-15, which moved this record from Tier 3 to Tier 1, increased the magnitude of the $\delta^{13}C$ anomaly by ~0.2‰, similar to the improvement expected from the global database.

Overall, our results are generally inconsistent with the Southern Ocean hypothesis. One prediction of this is hypothesis is that there should be larger $\delta^{13}C$ anomalies in the Southern Ocean and in regions of with AAIW and SAMW upwelling. Similar average $\delta^{13}C$ minima between the Southern Ocean and other ocean basins is inconsistent with this prediction. The uniformity between the anomalies in the WTP and the EEP is also inconsistent with the Southern Ocean hypothesis, as we would expect to find larger minima in the EEP, a dominant upwelling region, compared to the WTP convergence zone. Furthermore, the latitudinal trend of decreasing $\delta^{13}C$ anomalies towards higher latitudes in the Southern Ocean is opposite that expected due to upwelling of a $^{13}C$-depleted abyssal water mass south of the Polar Front. Finally, the explanation of the light isotopic signal carried by AAIW is conflicting with data showing positive anomalies at intermediate depths in several different regions of the ocean. Thus, the wide range of inconsistencies between our results and the Southern Ocean hypothesis suggests another mechanism is required to explain the deglacial carbon isotope minima.

The results of our spatial analysis of $\delta^{13}C$ minima are generally in agreement with the biological pump hypothesis. Similar $\delta^{13}C$ minima amongst ocean basins are in agreement with the SL15 model results. The ~0.2‰ discrepancy between the observed global $\delta^{13}C$ signal and model results is likely due to a combination of rising SSTs during the deglaciation and positive Southern Ocean anomalies simulated in the SL15 model. The uniformity of $\delta^{13}C$ minima between the WTP and EEP appears to be inconsistent with the biological pump hypothesis. A reduced efficiency of the biological pump should result in smaller minima in the EEP due to upwelling of relatively high $\delta^{13}C$ intermediate waters during HS1. The dominance of Tier 3 records in the WTP, however, may mask a larger $\delta^{13}C$ signal in this region compared to the Tier 1 dominated EEP. The latitudinal trend in Southern Ocean $\delta^{13}C$ minima agrees with the SL15

results of progressively larger anomalies north of 60°S. A weaker upper ocean $\delta^{13}C$ gradient during HS1 also supports the biological pump mechanism of reduced export of light carbon from the surface ocean to intermediate depths. The broad consistency between our findings and the SL15 model results suggests a weakened biological pump is the more likely explanation of the deglacial carbon isotope minima, and therefore the initial rise in $CO_2$ at the onset of the last deglaciation.

In order to further test the biological pump hypothesis, it is necessary to increase the resolution of Tier 3 records in the WTP for a more accurate comparison between minima in the EEP and WTP. Upgrading Tier 2 and Tier 3 age models from $\delta^{18}O$ stratigraphies to radiocarbon would help to definitively outline the HS1 time interval in each record. A meridional transect from 40°S-65°S is necessary to more accurately determine whether the latitudinal trend in the Southern Ocean is robust, and would specifically establish if positive $\delta^{13}C$ anomalies occurred at latitudes higher than 60°S. If future work can confirm the initial results presented in this thesis, it would suggest that the carbon isotope minima and rising atmospheric $CO_2$ during glacial terminations is triggered by AMOC-driven weakening of the biological pump, counter to conventional wisdom that terminations are initiated by upwelling of isotopically light carbon in the Southern Ocean.

APPENDIX

FIGURES

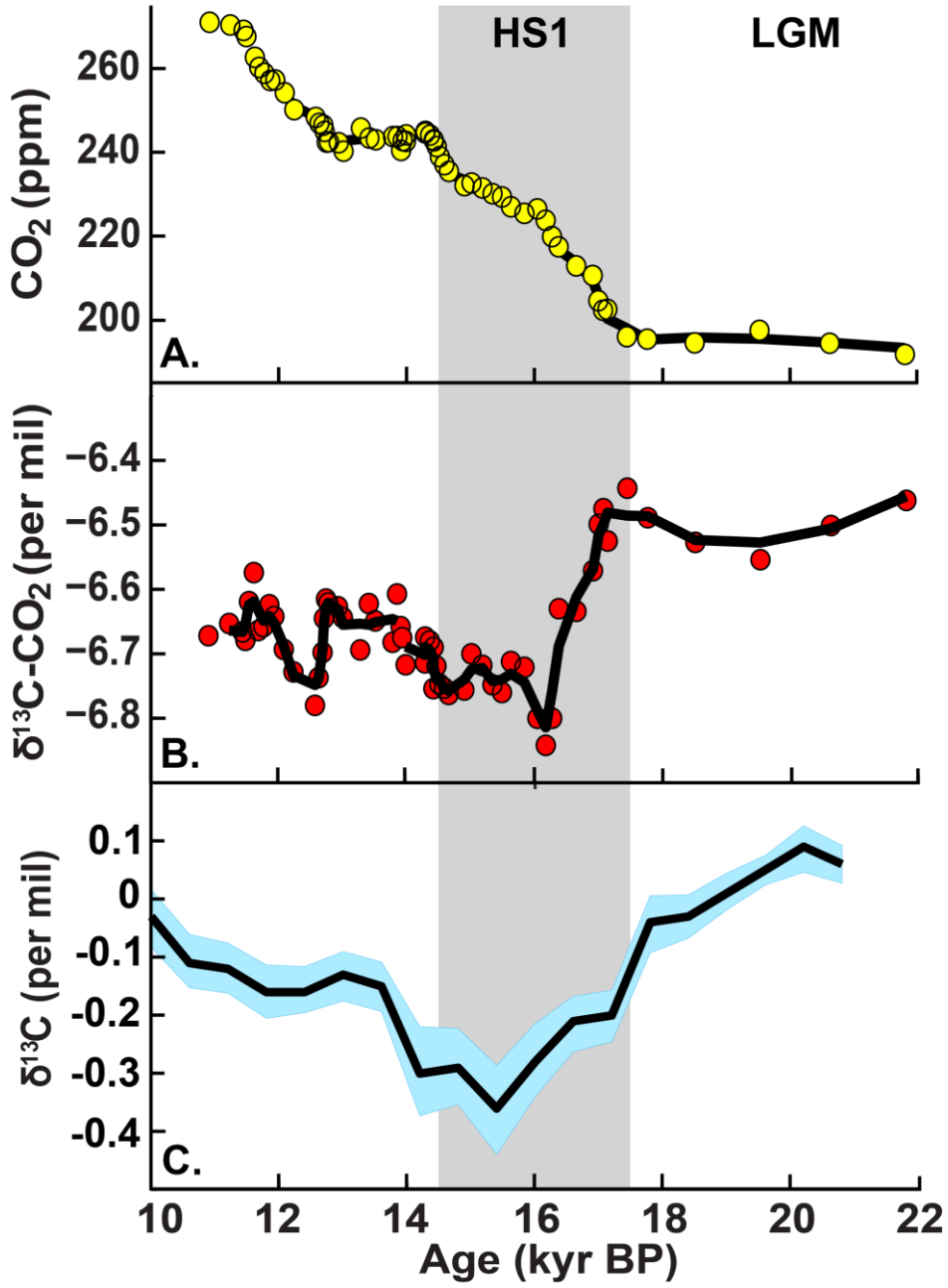


**Figure 1**. **Carbon cycle proxies for the last deglaciation**. **A**, concentration of atmospheric $CO_2$ (yellow markers, black line is a three-point running mean) from Taylor Glacier, Antarctica spanning the Last Glacial Maximum (LGM) through the deglaciation (Bauska et al., 2016). **B**, $\delta^{13}C$ of atmospheric $CO_2$ (red markers, black line is a three-point running mean) (Bauska et al., 2016). **C**, global stack of 21 planktonic $\delta^{13}C$ records ±1 SE (light blue area) (Tier 1, see methods) interpolated to a 600-yr resolution and averaged (this study). The shaded gray area represents Heinrich Stadial 1 (HS1: 14.5-17.5 kyr BP).

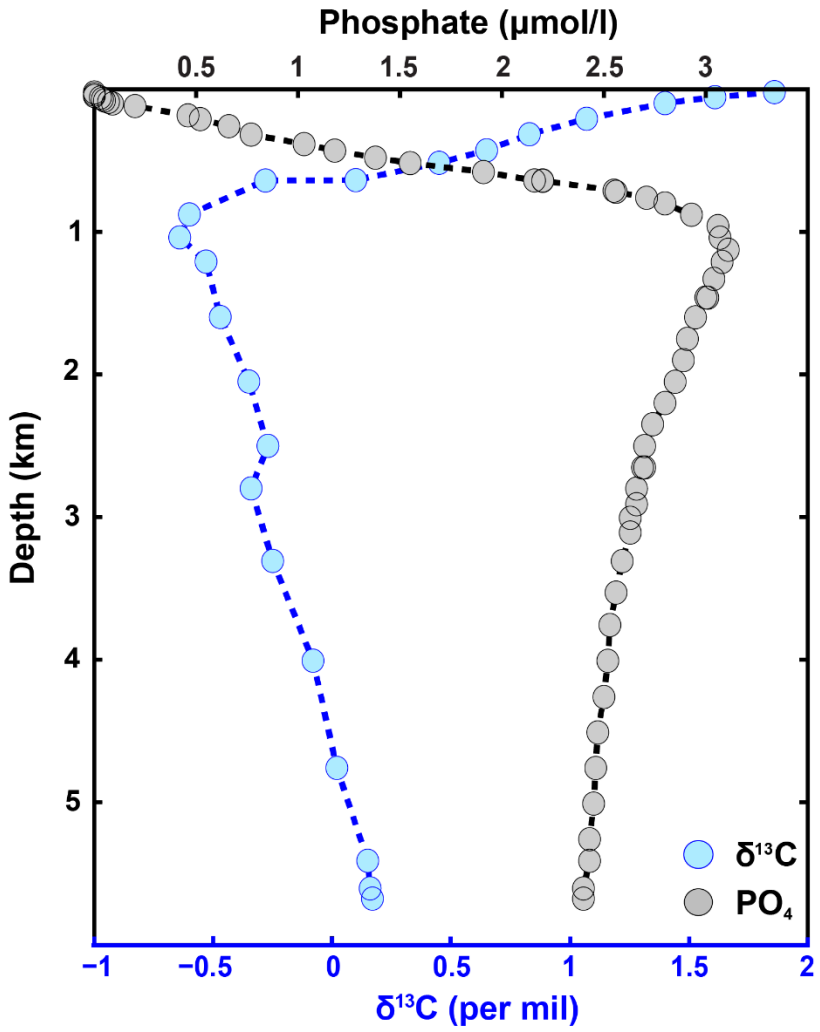


**Figure 2. Relationship between $\delta^{13}C$ of dissolved inorganic carbon (DIC) (blue) and phosphate (black) at GEOSECS station 213B in the North Pacific (30.97°N, 168.47°W).** The biological pump is the primary influence on ocean $\delta^{13}C$ of DIC. Photosynthesis in the surface ocean and respiration of organic matter at depth produces an inverse relationship between $\delta^{13}C$ of DIC and $PO_4$.

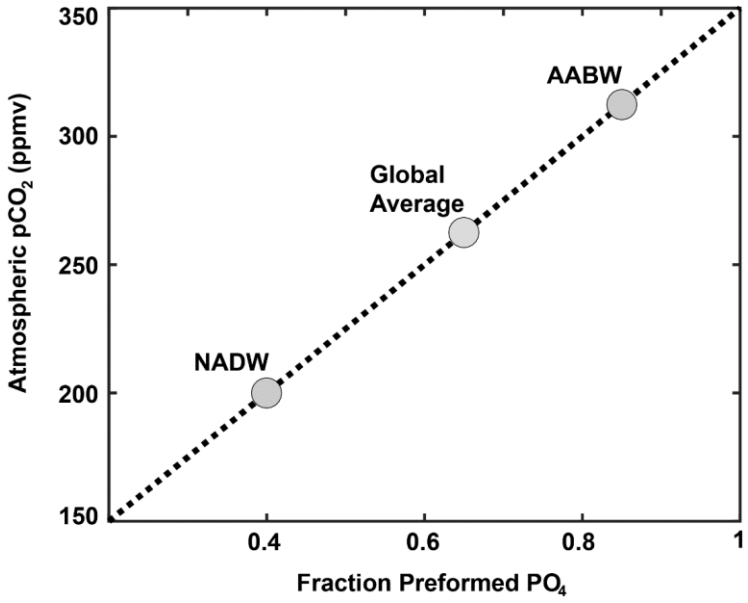


**Figure 3. Relationship between fraction of preformed $PO_4$ and atmospheric $CO_2$.** Simple theory and model results suggest the fraction of preformed $PO_4$ (i.e. $PO_4$ unused by photosynthesis) in the ocean is an indicator of the efficiency of the biological pump (Ito and Follows, 2005; Schmittner and Lund, 2015). North Atlantic Deep Water (NADW) has low preformed $PO_4$ and therefore represents efficient sequestration of $CO_2$ in the ocean via the biological pump. Antarctic Bottom Water (AABW) has a higher fraction of preformed $PO_4$, and represents a lost opportunity for biological productivity to sequester $CO_2$ in the abyss (after Ito and Follows, 2005).

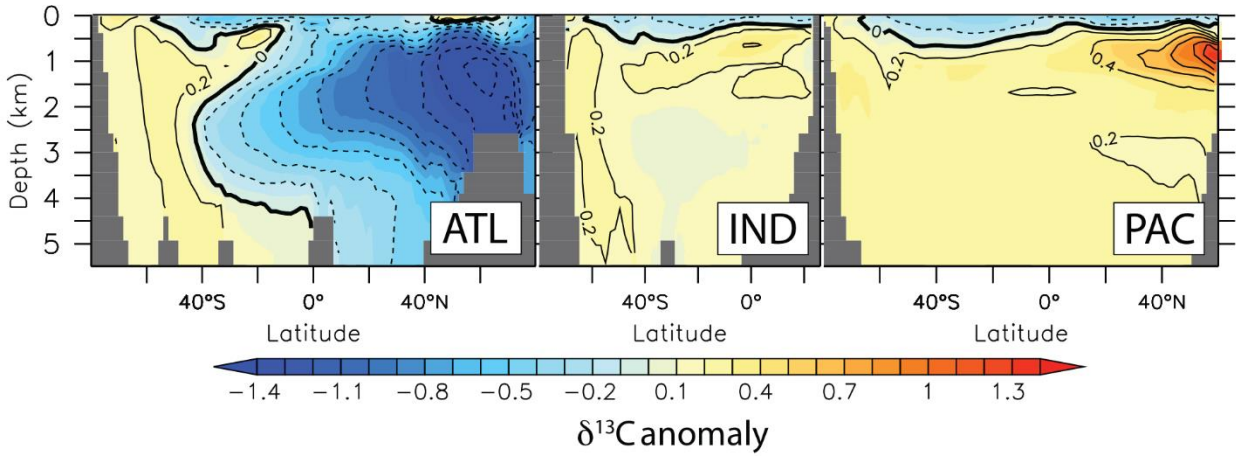


**Figure 4. Modeled $\delta^{13}C_{DIC}$ anomalies due to a reduction in the Atlantic Meridional Overturning Circulation (AMOC).** Plots show the $\delta^{13}C$ difference between preindustrial initial conditions and a collapsed AMOC state. Deep Atlantic anomalies are a direct consequence of the AMOC reduction while surface anomalies in the S. Atlantic, Indian, and Pacific are a result of a weakened biological pump. Note that positive anomalies at intermediate depths in the S. Atlantic, Indian, and Pacific Oceans are due to less export of organic carbon from surface waters. Model results from Schmittner and Lund (2015).

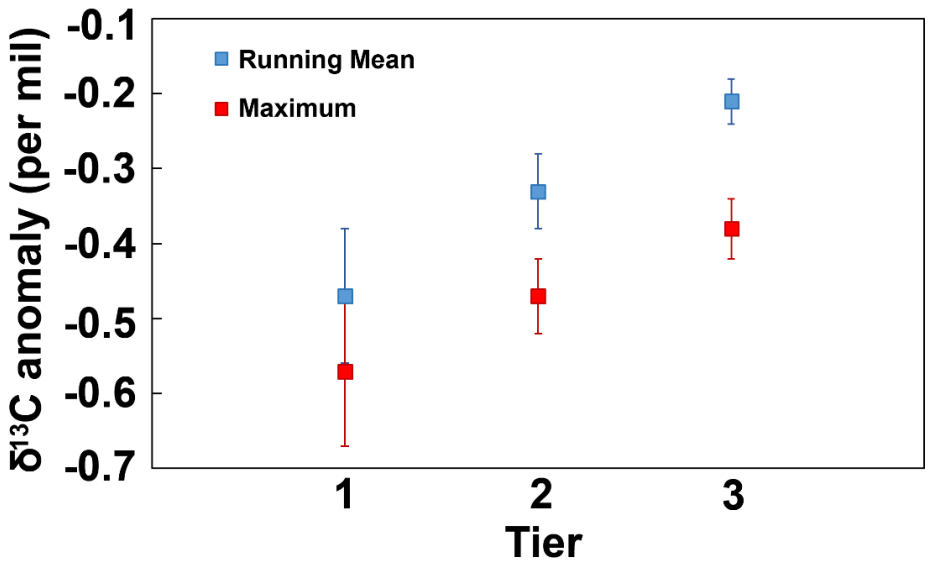


**Figure 5. Global $\delta^{13}C$ anomalies averaged by tier**. Maximum anomalies (red) represent the difference between averaged LGM $\delta^{13}C$ (19-23 kyr BP) and the lowest $\delta^{13}C$ value during the deglaciation (12-18 kyr BP). Running mean anomalies are calculated using a 3-point running mean. The running mean anomalies represent the difference between averaged LGM $\delta^{13}C$ (19-23 kyr BP) and the minimum $\delta^{13}C$ value of the 3-point running mean during the deglaciation (12-18 kyr BP). The error bars signify one standard error (1SE). Note that both Tier 1 and Tier 2 maximum and running mean anomalies are within one standard error of one another.

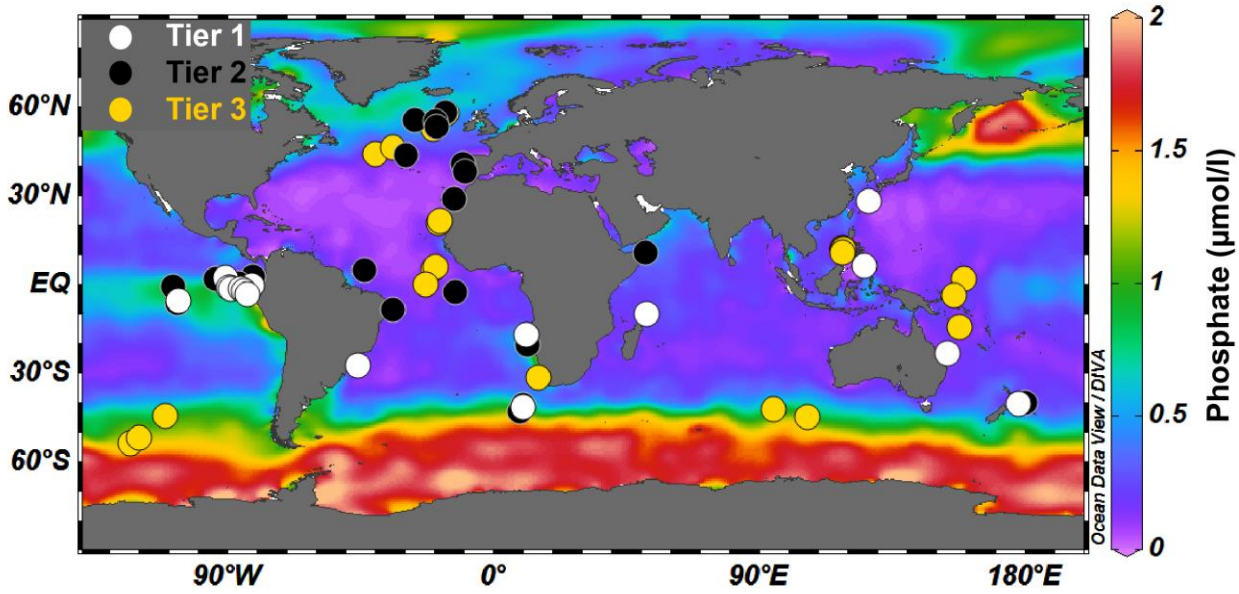


**Figure 6**. **Core location for planktonic $\delta^{13}C$ records.** Markers are superimposed on mean annual sea surface phosphate concentrations (µmol/l) from the World Ocean Atlas, 2001 (WOA01). Records are categorized into three tiers depending on the quality of the data, with Tier 1 representing the highest quality (see methods section for details). Map generated using ODV (https://odv.awi.de/).

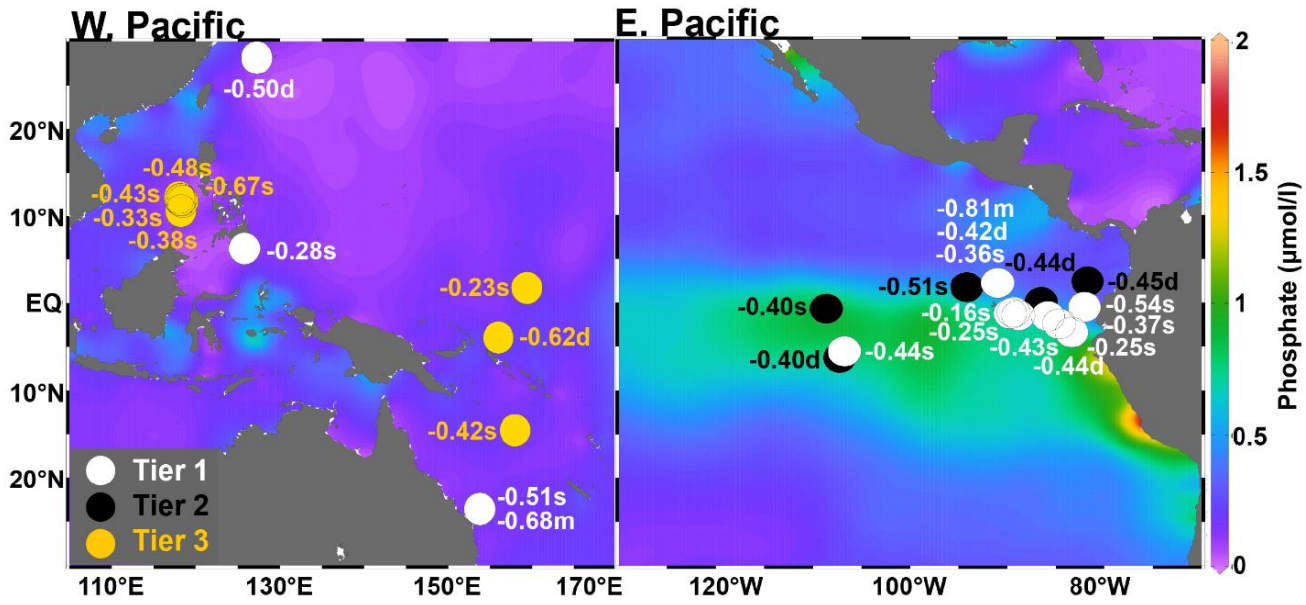


**Figure 7**. **Western and eastern tropical Pacific maximum deglacial $\delta^{13}C$ anomalies.** Anomalies are superimposed on annual sea surface phosphate concentrations (µmol/l) from the World Ocean Atlas, 2001 (WOA01). Maximum anomalies represent the difference between average LGM $\delta^{13}C$ (19-23 kyr BP) and the lowest $\delta^{13}C$ value during the deglaciation (12-18 kyr BP). Planktonic $\delta^{13}C$ records are categorized into three tiers depending on record quaility, with Tier 1 representing the highest quality data (see methods for details). Letters correspond to species of planktonic foraminifera: *G. sacculifer* (s), *N. dutertrei* (d), *G. menardii* (m), *G. inflata* (i), and *G. bulloides* (b). Map generated using ODV (https://odv.awi.de/).

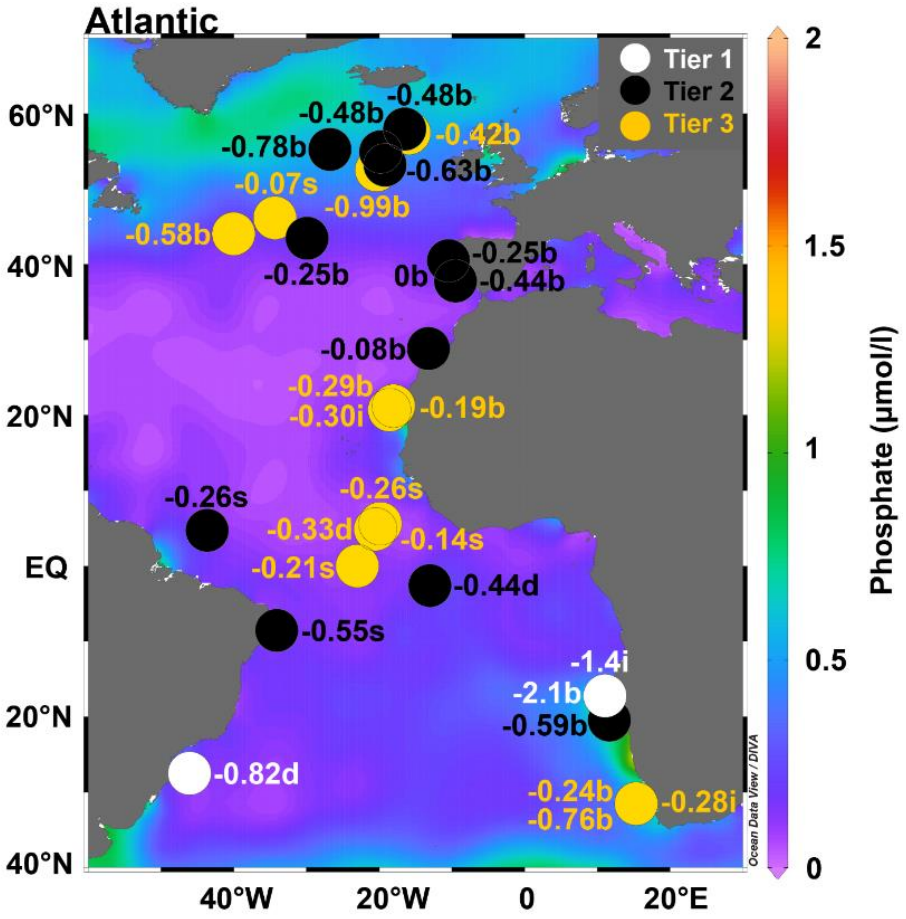


**Figure 8. Atlantic maximum deglacial $\delta^{13}C$ anomalies**. Plotting convention as described in Figure 7.

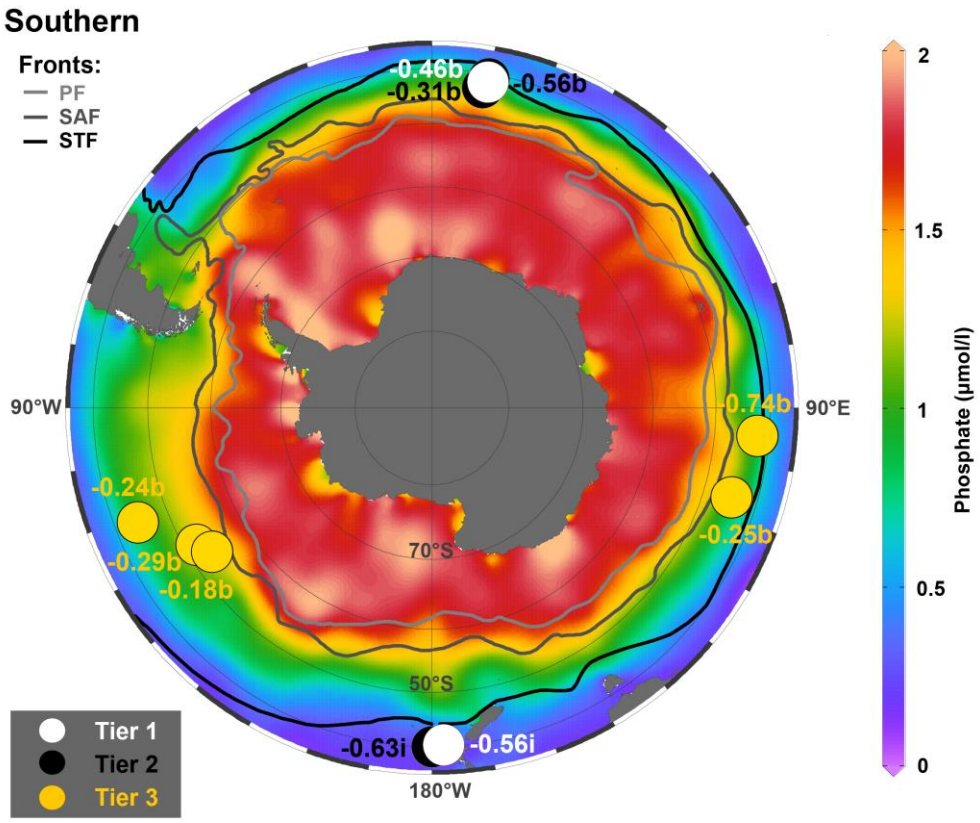


**Figure 9. Southern Ocean maximum deglacial $\delta^{13}C$ anomalies**. Plotting convention as described in Figure 7. The Southern Ocean fronts are as follows: Polar Front (PF), Subantarctic Front (SAF), and Subtropical Front (STF). Front data are from the Australian Antarctic Data Centre (original data from Orsi and Harris, 2001, updated 2015).

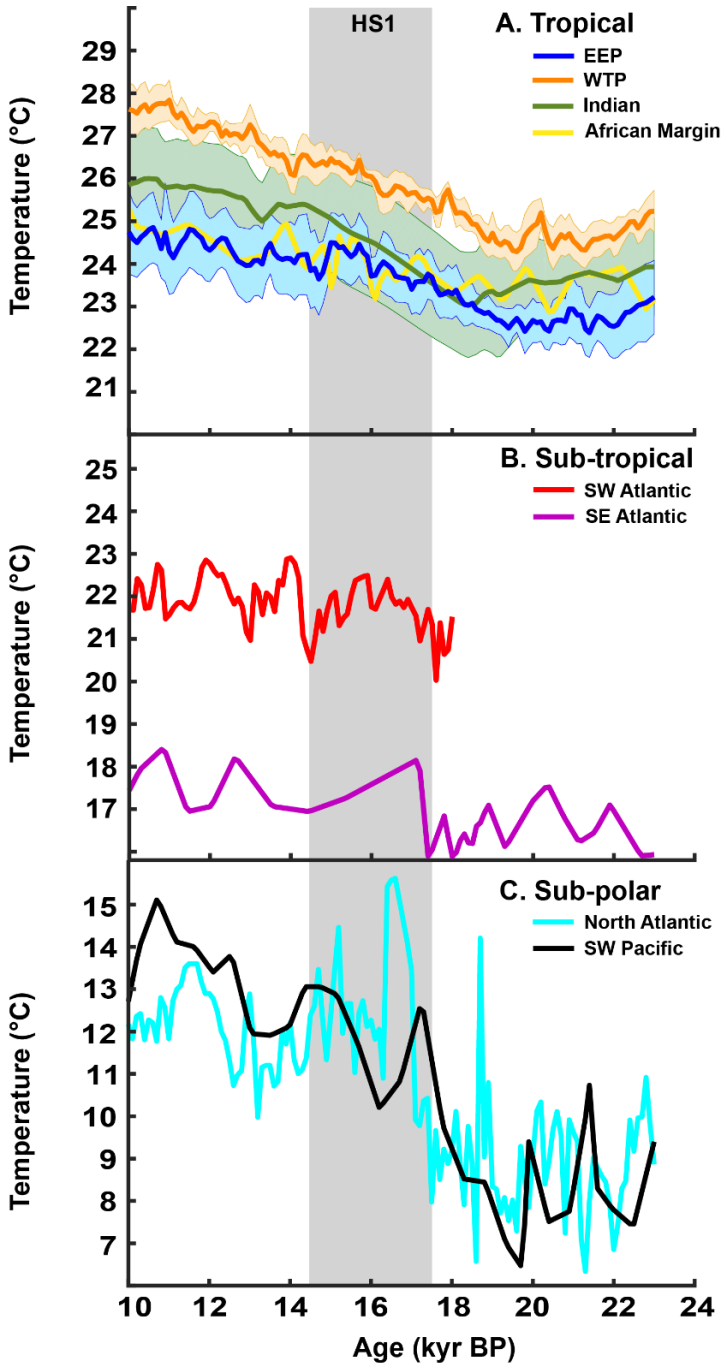


**Figure 10. Regional deglacial surface ocean temperature records.** Temperature records are categorized by latitude: **A**, Tropical **B**, Sub-tropical and **C**, Sub-polar. All temperature records are based on Mg/Ca analyses of planktonic foraminifera as reported by the original authors. Each record has an age resolution of more than one data point per kyr and an age model constrained by radiocarbon dates. Records from each region are interpolated to a 100-yr resolution. Averaged time series are provided for regions with more than one record (EEP n = 4; WTP n = 5; Indian n = 4). Error envelopes represent ±1 SE. The shaded vertical bar represents the Heinrich Stadial 1 time interval (14.5-17.5 kyr BP). Each y-axis spans 10°C, but note the different values for each subplot.

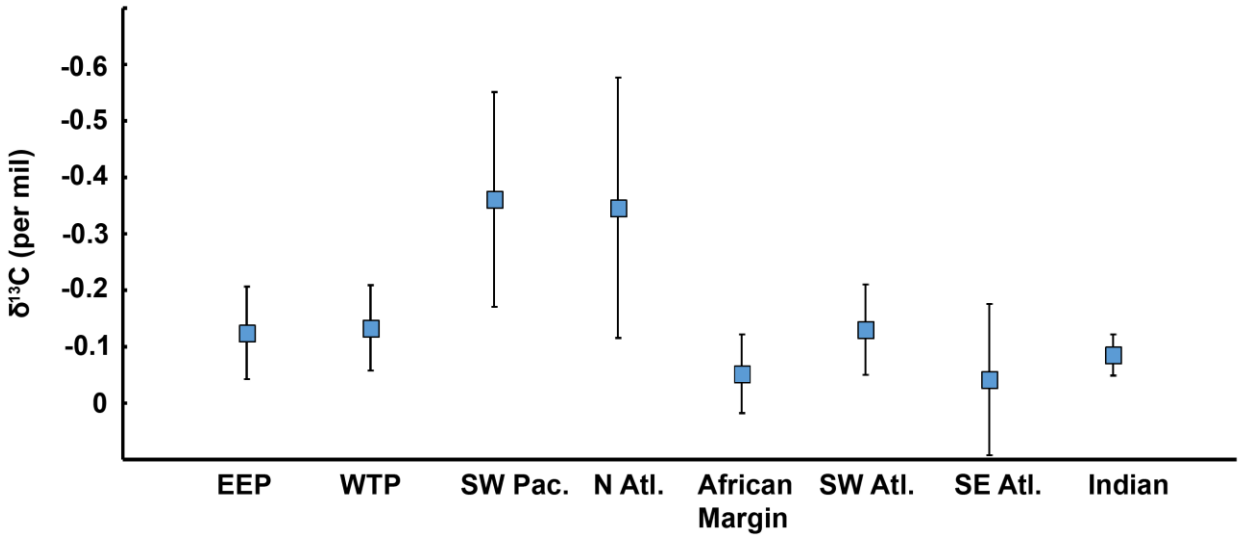


**Figure 11. Maximum potential fraction of $\delta^{13}C$ anomalies due to temperature dependent air-sea gas exchange**. At isotopic equilibrium, fractionation during air-sea gas exchange produces a relationship between surface ocean $\delta^{13}C$ and temperature of -0.1‰ per 1°C. Due to rising temperatures during the last deglaciation (Figure 10), a portion of the surface ocean $\delta^{13}C$ anomalies could be caused by the temperature dependent air-sea effect. The maximum temperature effect is estimated using the temperature differences between mean LGM and HS1 values for each region (Table 3) and the thermodynamic slope (-0.1‰/°C). Note that the estimates assume full equilibration between the surface ocean and atmosphere. Error bars represent ±1σ.

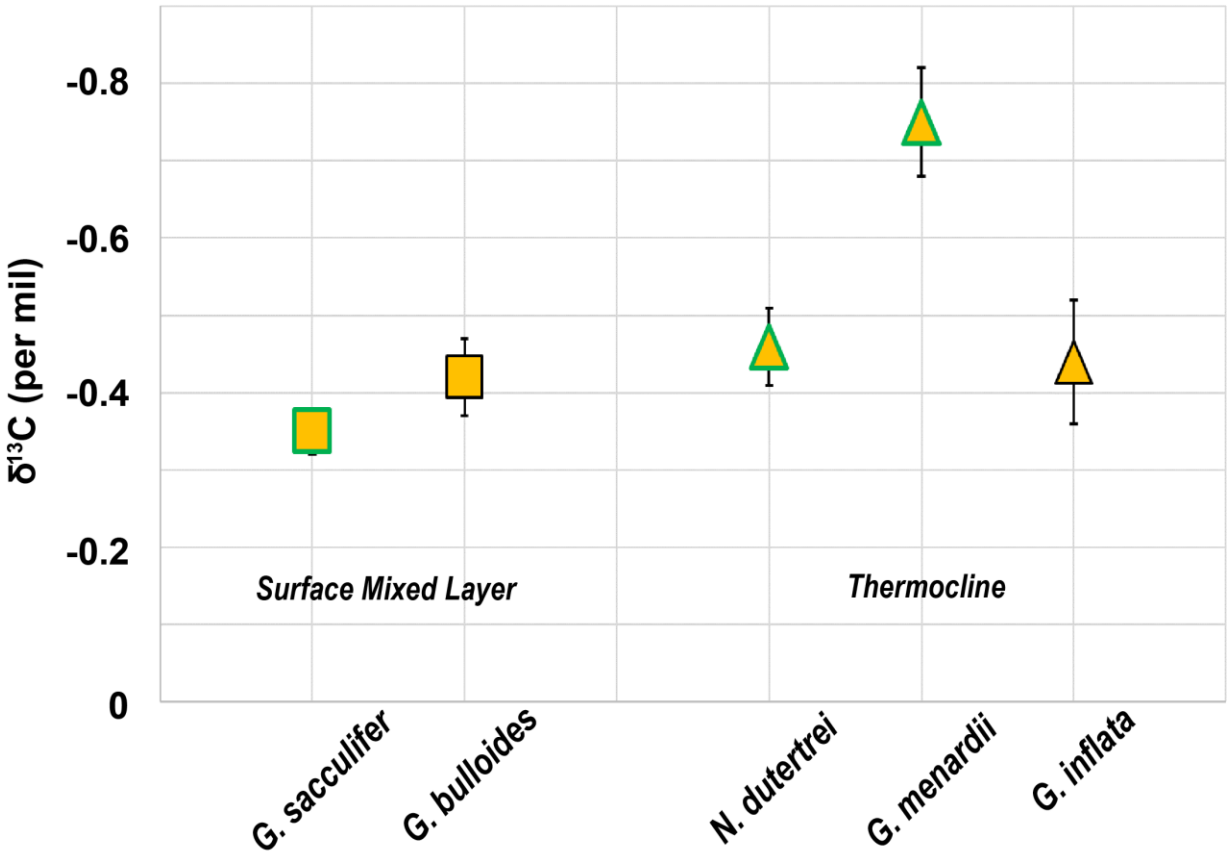


**Figure 12. Maximum average $\delta^{13}C$ anomaly for each planktonic foraminiferal species.** Squares represent the surface mixed layer species *G. sacculifer* (n = 25) and *G. bulloides* (n = 26), while triangles indicate thermocline-dwelling species *N. dutertrei* (n = 11), *G. menardii* (n = 2), and *G. inflata* (n = 4). A green outline signifies species with algal symbionts. The higher average anomaly for *G. menardii* relative to the other species is likely due to the lack of records from *G. menardii*. Error bars represent ±1SE.

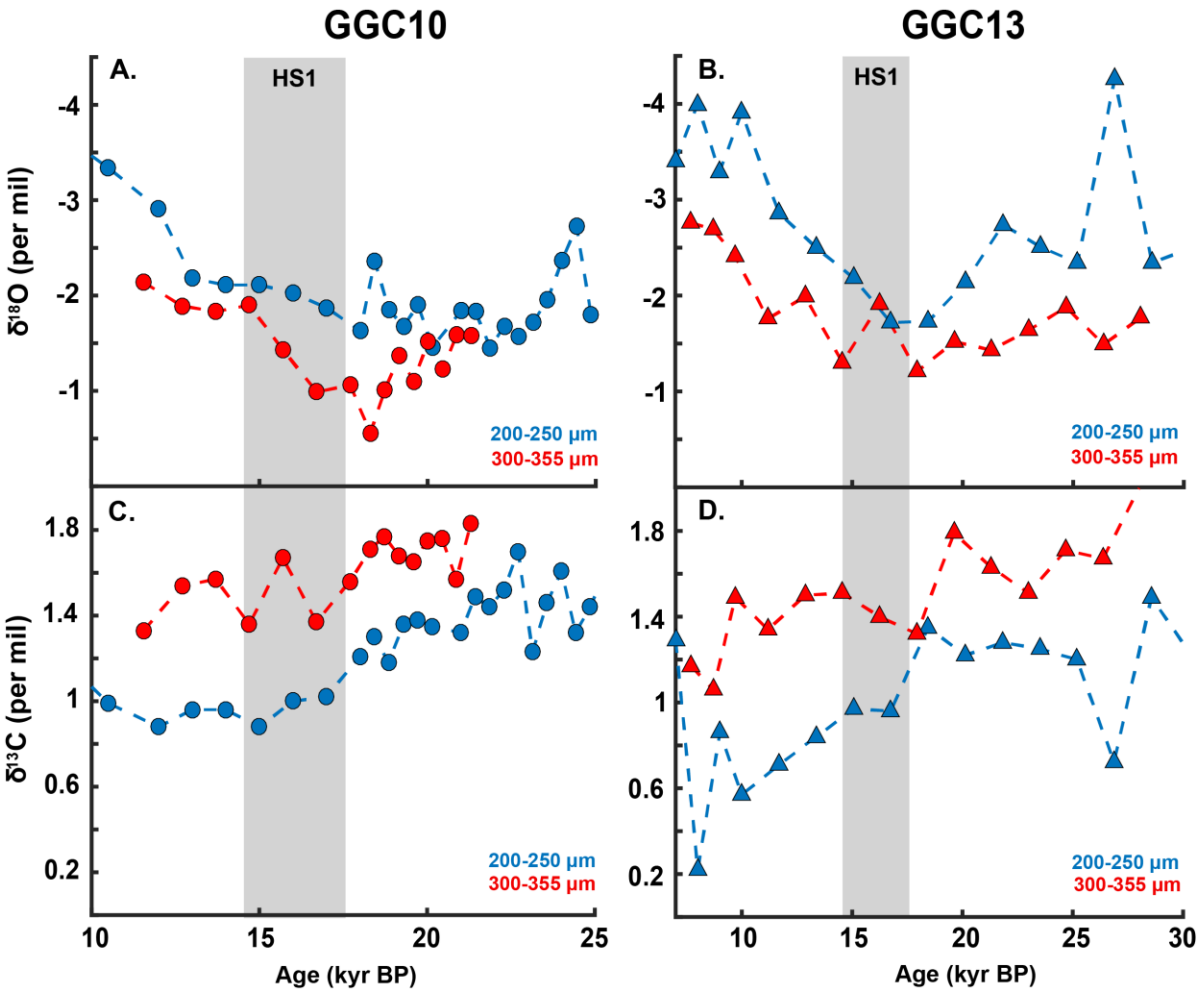


**Figure 13. Planktonic $\delta^{18}O$ and $\delta^{13}C$ results for GGC10 and GGC13 in the western tropical Pacific**. $\delta^{18}O$ results for GGC10 (**A**) and GGC13 (**B**) and corresponding $\delta^{13}C$ results for GGC10 (**C**) and GGC13 (**D**). Age models were generated by comparing $\delta^{18}O$ results to the global benthic $\delta^{18}O$ stack (Lisiecki and Raymo, 2005). $\delta^{18}O$ and $\delta^{13}C$ results for *G. sacculifer* from this study (red) are offset from the previous results by Thunell et al. (1992) (blue). These results demonstrate issues with analyzing different size fractions of symbiont-bearing planktonic foraminifera. For GGC10 (circles), the mean $\delta^{18}O$ offset is -0.58 ± 0.07‰ (1SE) and mean $\delta^{13}C$ offset is -0.48 ± 0.02‰ (1SE). For GGC13 (triangles), the mean $\delta^{18}O$ offset is -0.93 ± 0.08‰ (1SE) and mean $\delta^{13}C$ offset is -0.53 ± 0.03‰ (1SE). The outlier at ~27 kyr BP contributes to the large $\delta^{18}O$ and $\delta^{13}C$ offsets between the different datasets. The shaded vertical bars represent the HS1 time interval.

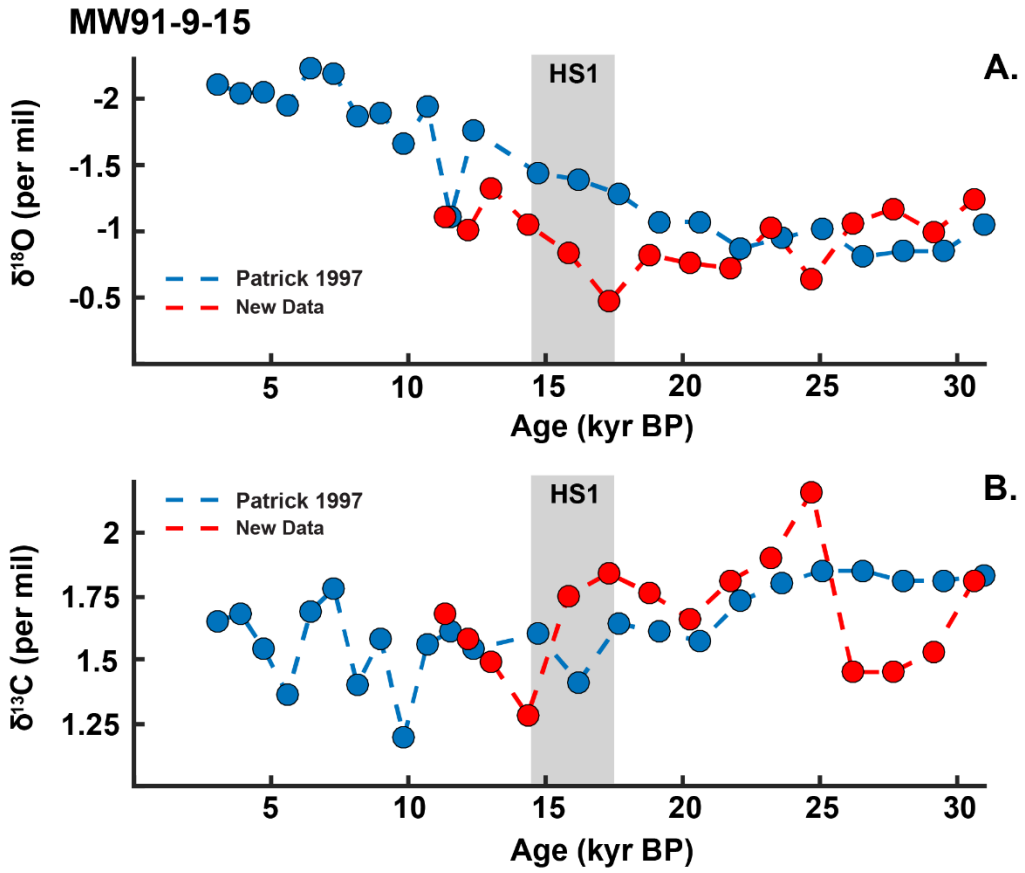


**Figure 14. Planktonic $\delta^{18}O$ and $\delta^{13}C$ results for MW91-9-15.** *G. sacculifer* $\delta^{18}O$ (**A**) and $\delta^{13}C$ (**B**) results from this study (red) compared to the previous results from Patrick et al. (1997) (blue). The age model is based on published radiocarbon dates (citation) recalibrated using Calib 7.1 (citation). The shaded gray areas represent Heinrich Stadial 1. Both analyses used the 300-355 μm size fraction of *G. sacculifer*. The mean offset between the $\delta^{18}O$ records is -0.22 ± 0.05‰ (1SE), while that for $\delta^{13}C$ is negligible (0.003 ± 0.037‰, 1SE).

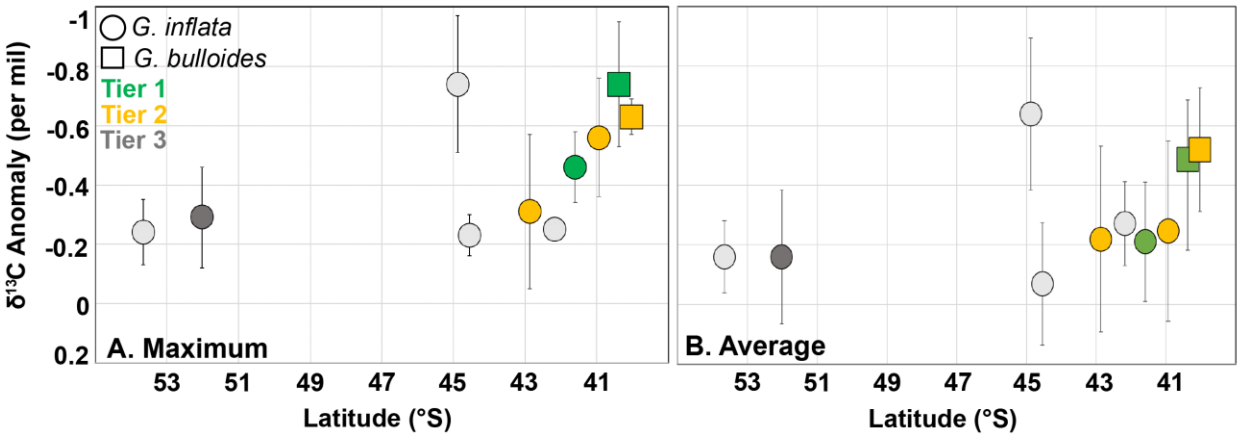


**Figure 15. Southern Ocean $\delta^{13}C$ anomalies plotted versus latitude.** Maximum (**A**) and average (**B**) $\delta^{13}C$ anomalies increase in magnitude with decreasing latitude. Tier 1 (green) and Tier 2 (yellow) anomalies were determined using a time window of 16-17.5 kyr BP, the early portion HS1. Tier 3 (gray) $\delta^{13}C$ anomalies are averaged using a 12-18 kyr BP time period due to their very low resolution, with only one record having more than one data point every 2 kyr (dark gray circle). Error bars represent 1σ.

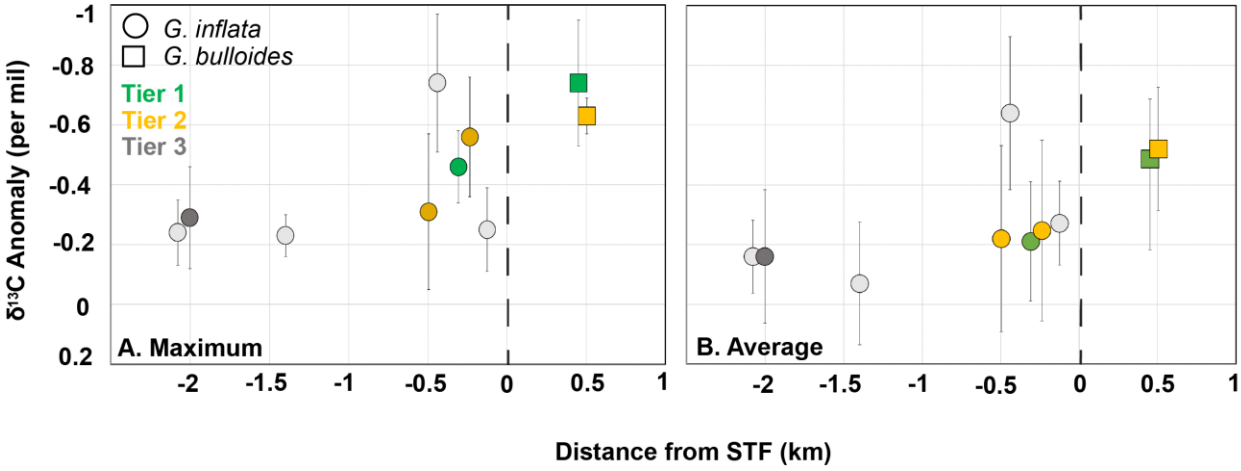


**Figure 16. Southern Ocean $\delta^{13}C$ anomalies are plotted against distance from the subtropical (STF).** Plotting convention is the same as in Figure 15.

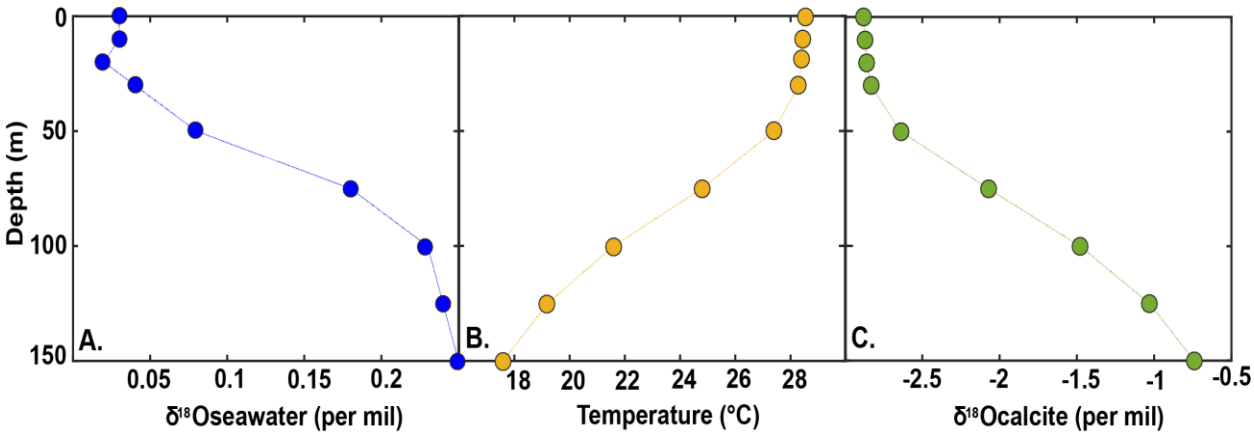


**Figure 17. Predicted $\delta^{18}O_{calcite}$ depth profile using modern data located near GGC10 and GGC13 in the western tropical Pacific (WTP). A**, calculated $\delta^{18}O_{seawater}$ depth profile based on the linear regression $\delta^{18}O_{seawater}$ = 0.21*salinity – 7.1 calculated using modern salinity and $\delta^{18}O_{seawater}$ data from 0-100 m in the WTP (23°S-23°N, 110°E-170°W) from the Global Seawater Oxygen-18 Database (http://data.giss.nasa.gov/o18data/) and a modern salinity profile in the WTP (World Ocean Atlas 2001, 11.5°N, 118.5°E). **B**, vertical temperature profile from the same site as the salinity profile (World Ocean Atlas 2001, 11.5°N, 118.5°E) **C**, Predicted $\delta^{18}O_{calcite}$ depth profile in the WTP estimated using data in panels A and B and the paleothermometry equation for *G. sacculifer* (Spero et al., 2003).

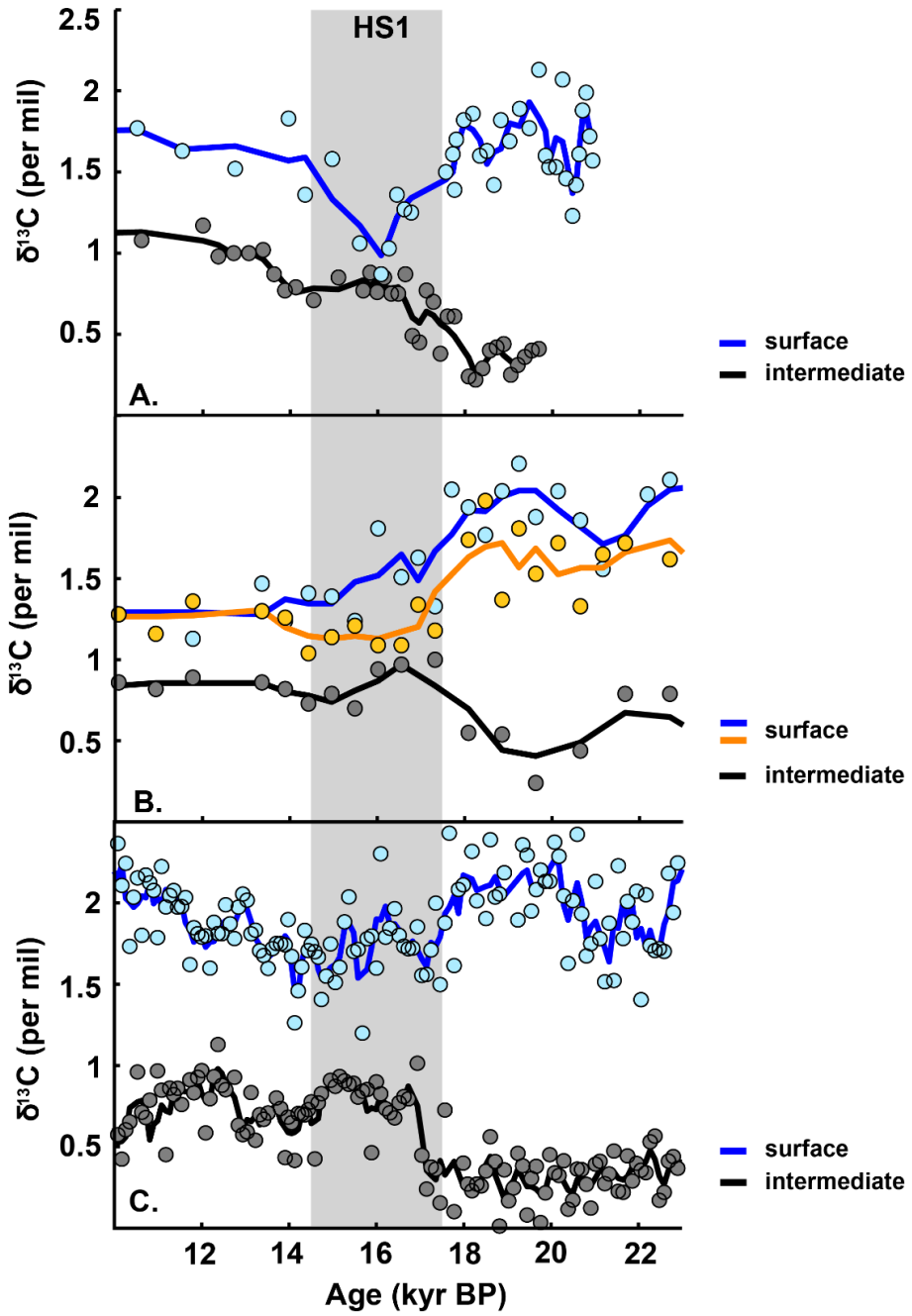


**Figure 18. Surface and intermediate depth $\delta^{13}C$ records during HS1. A**, Records from the Brazil Margin. Surface water record is from planktonic foraminiferal species *N. dutertrei* (Hertzberg et al., submitted) Intermediate record is from benthic species *Cibicidoides spp.* at 1100 m water depth (Lund et al., 2015). **B**, Records from the SW Pacific. Surface records are from planktonic species *G. menardii* (blue) and *G. sacculifer* (orange). Intermediate record is from *Cibicidoides spp.* at 990 m water depth (Bostock et al., 2004). **C**, Southern Ocean records. Surface water records are from planktonic species *G. bulloides*. Intermediate record is from *Cibicidoides spp.* at 990 m water depth (Pahnke et al., 2005). Lines represent a 3-point running mean, circles denote actual values. Gray vertical bar indicates HS1.

TABLES

**Table A1. ΔR values for the calibration of all Tier 1 radiocarbon dates.** ΔR values are determined for each core by averaging the 10 closest known ΔR values from the marine reservoir correction database. An error of ±200 years is applied to each ΔR.

| Core | Latitude | Longitude | ΔR |
|---|---|---|---|
| DGKS9603 | 28.15 | 127.27 | 24 |
| MD98-2181 | 6.3 | 125.83 | 28 |
| TR163-19 | 2.26 | -90.95 | 125 |
| TR163-19 | 2.26 | -90.95 | 125 |
| TR163-19 | 2.26 | -90.95 | 125 |
| V19-27 | -0.47 | -82.01 | 62 |
| V21-29 | -1.05 | -89.35 | 96 |
| V21-30 | -1.21 | -89.68 | 125 |
| RC8-102 | -1.42 | -88.85 | 135 |
| RC11-238 | -1.52 | -85.82 | 95 |
| V19-28 | -2.37 | -84.65 | 85 |
| V19-30 | -3.35 | -83.35 | 122 |
| V21-40 | -5.52 | -106.77 | 70 |
| WIND 28K | -10.15 | 51.77 | 165 |
| GEOB 1023-5 | -17.16 | 11.01 | 180 |
| GEOB 1023-5 | -17.16 | 11.01 | 180 |
| FR01/97-12 | -23.58 | 153.79 | 11 |
| FR01/97-12 | -23.58 | 153.79 | 11 |
| 78GGC | -27.48 | -46 | 33 |
| MD97-2121 | -40.38 | 177.99 | 12 |
| RC11-83 | -41.6 | 9.8 | 158 |

**Table A2. Atlantic Ocean $\delta^{13}C$ records with potentially positive HS1 anomalies.** These $\delta^{13}C$ records have periods of rising and falling $\delta^{13}C$ during the deglaciation, suggesting $\delta^{13}C$ at these locations could be increasing or decreasing during HS1 depending on the age model.

| Core | Latitude | Longitude | Species | Tier | Reference |
|---|---|---|---|---|---|
| CHN82-20 | 43.50 | -29.87 | *G. bulloides* | 2 | Dephi |
| NO82-13 | 40.53 | -10.43 | *G. bulloides* | 2 | Labeyrei, 1996 |
| GEOB4240-2 | 28.89 | -13.22 | *G. bulloides* | 2 | Freudenthal et al., 2002 |
| GIK23418-8 | 52.55 | -20.33 | *G. bulloides* | 3 | Jung and Sarnthein, 2003d |
| ODP658C | 20.75 | -18.58 | *G. bulloides* | 3 | Zhao et al., 1995 |
| ODP658C | 20.75 | -18.58 | *G. inflata* | 3 | Zhao et al., 1995 |
| GIK16030-1 | 21.23 | -18.05 | *G. bulloides* | 3 | Sarnthein et al., 1994 |

**Table A3. Core location of Mg/Ca temperature records.** *denotes record from Shakun et al. (2012) temperature compilation.

| Core | Latitude | Longitude | Region | Reference |
|---|---|---|---|---|
| V21-30 | -1.2 | -89.7 | EEP | Koutavas et al., 2002; Nurnberg et al., 1996* |
| TR163-22 | 0.5 | -92.4 | EEP | Lea et al., 2006; Dekens et al., 2002* |
| ME0005A-43JC | 7.9 | -83.6 | EEP | Benway et al., 2006; Anand et al., 2003* |
| ODP1240 | 0.0 | -86.5 | EEP | Pena et al., 2008 |
| ODP 1144 | 20.1 | 117.6 | WTP | Wei et al., 2007; Nurberg et al., 2000* |
| MD01-2390 | 6.6 | 113.4 | WTP | Steinke et al., 2008; Dekens et al., 2002* |
| MD9821-62 | -4.7 | 117.9 | WTP | Visser et al., 2003; Hastings et al., 2001* |
| MD98-2165 | -9.7 | 118.4 | WTP | Levi et al., 2007; Dekens et al., 2002* |
| MD01-2378 | -13.1 | 121.8 | WTP | Xu et al., 2008; Anand et al., 2003* |
| MD97-2120 | -45.5 | 174.9 | SW Pacific | Pahnke et al., 2003 |
| MD01-2461 | 51.8 | -12.9 | North Atlantic | Peck et al., 2008* |
| GeoB9526 | 12.4 | -18.1 | NW African Margin | Zarriess et al., 2011 |
| GeoB6211-2 | -32.5 | -50.2 | SW Atlantic | Chiessi et al., 2015 |
| MD02-2594 | -34.1 | 17.3 | SE Atlantic | Martinez-Mendez et al., 2010 |
| GeoB12615-4 | -7.1 | 39.8 | Indian | Romahn et al., 2014 |
| AAS9-21 | 14.5 | 72.7 | Indian | Govil and Naidu, 2010 |
| WIND28K | -10.2 | 51.8 | Indian | Johnstone et al., 2014 |

**Table A4. Pacific Ocean $\delta^{13}C$ running mean and maximum anomalies.** Corresponding core, location, species used for $\delta^{13}C$ record, tier, and reference are listed.

| Core | Latitude | Longitude | Species | Tier | Running Mean Anomaly (‰) | Maximum Anomaly (‰) | Reference |
|---|---|---|---|---|---|---|---|
| DGKS9603 | 28.2 | 127.3 | *N. dutertrei* | 1 | -0.43 | -0.5 | Li et al., 2002 |
| MD98-2181 | 6.3 | 125.8 | *G. sacculifer* | 1 | -0.2 | -0.28 | Stott et al., 2002 |
| TR163-19 | 2.3 | -91.0 | *N. dutertrei* | 1 | -0.3 | -0.42 | Spero et al., 2003 |
| TR163-19 | 2.3 | -91.0 | *G. sacculifer* | 1 | -0.23 | -0.36 | Spero et al., 2003 |
| TR163-19 | 2.3 | -91.0 | *G. menardii* | 1 | -0.74 | -0.81 | Spero et al., 2003 |
| V19-27 | -0.5 | -82.0 | *G. sacculifer* | 1 | -0.41 | -0.54 | Koutavas and Lynch-Stieglitz, 2003 |
| V21-29 | -1.1 | -89.4 | *G. sacculifer* | 1 | -0.15 | -0.25 | Koutavas and Lynch-Stieglitz, 2003 |
| V21-30 | -1.2 | -89.7 | *G. sacculifer* | 1 | -0.27 | -0.43 | Koutavas and Lynch-Stieglitz, 2003 |
| RC8-102 | -1.4 | -88.9 | *G. sacculifer* | 1 | -0.09 | -0.16 | Koutavas and Lynch-Stieglitz, 2003 |
| RC11-238 | -1.5 | -85.8 | *G. sacculifer* | 1 | -0.35 | -0.37 | Koutavas and Lynch-Stieglitz, 2003 |
| V19-28 | -2.4 | -84.7 | *G. sacculifer* | 1 | -0.12 | -0.25 | Koutavas and Lynch-Stieglitz, 2003 |
| V19-30 | -3.4 | -83.4 | *N. dutertrei* | 1 | -0.42 | -0.44 | Shackleton and Pisias, 1985 |
| V21-40 | -5.5 | -106.8 | *G. sacculifer* | 1 | -0.37 | -0.44 | Koutavas and Lynch-Stieglitz, 2003 |
| FR01/97-12 | -23.6 | 153.8 | *G. sacculifer* | 1 | -0.47 | -0.51 | Bostock et al., 2004 |
| FR01/97-12 | -23.6 | 153.8 | *G. menardii* | 1 | -0.57 | -0.68 | Bostock et al., 2004 |
| V19-25 | 2.5 | -81.7 | *N. dutertrei* | 2 | -0.44 | -0.45 | Delphi |
| RC13-138 | 1.8 | -94.1 | *G. sacculifer* | 2 | -0.27 | -0.51 | Delphi |
| Y69-71P | 0.1 | -86.5 | *N. dutertrei* | 2 | -0.32 | -0.44 | Clark et al., 2004 |
| RC10-65 | -0.7 | -108.6 | *G. sacculifer* | 2 | -0.13 | -0.4 | Delphi |
| Y71-09-115 | -6.3 | -107.2 | *N. dutertrei* | 2 | -0.32 | -0.4 | Hertzberg et al., in prep |
| GGC-6 | 12.2 | 118.1 | *G. sacculifer* | 3 | -0.17 | -0.33 | Thunell et al., 1992 |
| GGC-10 | 11.9 | 118.2 | *G. sacculifer* | 3 | -0.36 | -0.43 | Thunell et al., 1992 |
| GGC-12 | 11.9 | 118.3 | *G. sacculifer* | 3 | -0.19 | -0.48 | Thunell et al., 1992 |
| GGC-13 | 11.7 | 118.5 | *G. sacculifer* | 3 | -0.53 | -0.67 | Thunell et al., 1992 |
| GGC-11 | 10.6 | 118.3 | *G. sacculifer* | 3 | -0.06 | -0.38 | Thunell et al., 1992 |
| RC17-177 | 1.8 | 159.5 | *G. sacculifer* | 3 | -0.18 | -0.23 | Shackleton et al., 1992 |
| WP7 | -3.9 | 156.0 | *N. dutertrei* | 3 | -0.39 | -0.62 | Li et al., 2011 |
| MW91-15 | -14.5 | 158.0 | *G. sacculifer* | 3 | -0.09 | -0.23 | Patrick and Thunell, 1997 |

**Table A5. Atlantic Ocean $\delta^{13}C$ running mean and maximum anomalies.** Corresponding location, core, species used for $\delta^{13}C$ record, tier, and reference are listed.

| Core | Latitude | Longitude | Species | Tier | Running Mean Anomaly (‰) | Maximum Anomaly (‰) | Reference |
|---|---|---|---|---|---|---|---|
| KNR159-5-78 | -27.5 | -46.0 | *N. dutertrei* | 1 | -0.71 | -0.82 | Hertzberg et al., submitted |
| GEOB 1023-5 | -17.2 | 11.0 | *G. bulloides* | 1 | -1.82 | -2.1 | Schneider et al., 1992 |
| GEOB 1023-5 | -17.2 | 11.0 | *G. inflata* | 1 | -1.14 | -1.41 | Schneider et al., 1992 |
| BOFS17K | 58.0 | -16.5 | *G. bulloides* | 2 | -0.43 | -0.48 | Lowry et al., 1994 |
| GIK17049-6 | 55.3 | -26.7 | *G. bulloides* | 2 | -0.52 | -0.78 | Jung and Sarnthein, 2003e |
| GIK23419-8 | 55.0 | -19.8 | *G. bulloides* | 2 | -0.37 | -0.48 | Jung and Sarnthein, 2003a |
| GIK23415-9 | 53.2 | -19.1 | *G. bulloides* | 2 | -0.52 | -0.63 | Jung and Sarnthein, 2003c |
| CHN82-20 | 43.5 | -29.9 | *G. bulloides* | 2 | -0.24 | -0.25 | Delphi |
| NO82-13 | 40.5 | -10.4 | *G. bulloides* | 2 | -0.15 | -0.25 | Labeyrei, 1996 |
| PO200-10-8-2.97 | 37.8 | -9.5 | *G. bulloides* | 2 | -0.34 | -0.44 | Abrantes et al., 1998 |
| PO200-10-6-2 | 37.6 | -9.9 | *G. bulloides* | 2 | 0 | 0 | Abrantes et al., 1998 |
| GEOB4240-2 | 28.9 | -13.2 | *G. bulloides* | 2 | 0.14 | -0.08 | Freudenthal et al., 2002 |
| KNR110-43PC | 4.7 | -43.7 | *G. sacculifer* | 2 | -0.22 | -0.26 | Curry and Crowley, 1987 |
| GS7309-6PC | -2.5 | -13.0 | *N. dutetrei* | 2 | -0.29 | -0.44 | Loubere et al., 2011 |
| GeoB2204-2 | -8.5 | -34.0 | *G. sacculifer* | 2 | -0.32 | -0.55 | Durkoop et al., 1997 |
| V19-258 | -20.4 | 11.6 | *G. bulloides* | 2 | -0.36 | -0.59 | Lynch-Stieglitz et al., 2006 |
| SU90-11 | 44.1 | -40.0 | *G. bulloides* | 3 | -0.14 | -0.58 | Labeyrie et al., 1995 |
| ODP site 851 | 46.2 | -34.3 | *G. sacculifer* | 3 | -0.04 | -0.07 | Cannariato and Ravelo, 1997 |
| EN066-38GGC | 4.9 | -20.5 | *N. dutertrei* | 3 | -0.19 | -0.33 | Curry and Crowley, 1987 |
| EN066-38GGC | 4.9 | -20.5 | *G. sacculifer* | 3 | -0.07 | -0.14 | Curry and Crowley, 1987 |
| GIK23418-8 | 52.6 | -20.3 | *G. bulloides* | 3 | -0.62 | -0.99 | Jung anad Sarnthein, 2003d |
| GIK13519-1 | 5.7 | -19.9 | *G. sacculifer* | 3 | -0.15 | -0.26 | Sarnthein et al., 1984 |
| ODP658C | 20.8 | -18.6 | *G. bulloides* | 3 | -0.08 | -0.29 | Zhao et al., 1995 |
| ODP658C | 20.8 | -18.6 | *G. inflata* | 3 | -0.14 | -0.3 | Zhao et al., 1995 |
| GIK16030-1 | 21.2 | -18.1 | *G. bulloides* | 3 | 0.05 | -0.19 | Sarnthein et al., 1994 |
| ODP982 | 57.5 | -15.9 | *G. bulloides* | 3 | -0.2 | -0.42 | Venz et al., 1999 |
| 175-1087A-1H | -31.5 | 15.3 | *G. bulloides* | 3 | -0.13 | -0.24 | Pierre et al., 2001 |
| 175-1087A-1H | -31.5 | 15.3 | *G. inflata* | 3 | -0.08 | -0.28 | Pierre et al., 2001 |
| V19-236 | -33.9 | 17.6 | *G. bulloides* | 3 | -0.38 | -0.76 | Lynch-Stieglitz et al., 2006 |
| 12PC51 | 0.0 | -23.0 | *G. sacculifer* | 3 | -0.1 | -0.21 | Sikes and Keigwin, 1994 |

**Table A6. Southern Ocean $\delta^{13}C$ running mean and maximum anomalies.** Corresponding location, core, species used for $\delta^{13}C$ record, tier, and reference are listed.

| Core | Latitude | Longitude | Species | Tier | Running Mean Anomaly (‰) | Maximum Anomaly (‰) | Reference |
|---|---|---|---|---|---|---|---|
| MD97-2121 | -40.4 | 178.0 | *G. inflata* | 1 | -0.43 | -0.56 | Carter et al., 2008 |
| RC11-83 | -41.6 | 9.8 | *G. bulloides* | 1 | -0.39 | -0.46 | Charles et al., 1996 |
| CHAT10K-1 | -40.0 | 180.0 | *G. inflata* | 2 | -0.52 | -0.63 | McCave et al., 2008 |
| TTN057-6 | -42.9 | 9.0 | *G. bulloides* | 2 | -0.16 | -0.31 | Hodell et al., 2003 |
| ODP1089 | -40.9 | 9.9 | *G. bulloides* | 2 | -0.36 | -0.56 | Hodell et al., 2003 |
| RC12-225 | -53.7 | -123.1 | *G. bulloides* | 3 | -0.12 | -0.18 | Rickaby and Elderfield, 1999 |
| ELT49-21 | -42.2 | 94.9 | *G. bulloides* | 3 | -0.18 | -0.25 | Howard and Prell, 1992 |
| ELT45-29 | -44.9 | 106.5 | *G. bulloides* | 3 | -0.63 | -0.74 | Howard and Prell, 1992 |
| E20-18 | -44.6 | -111.3 | *G. bulloides* | 3 | -0.07 | -0.24 | Loubere et al., 2008 |
| E21-15 | -52.0 | -120.0 | *G. bullodies* | 3 | -0.18 | -0.29 | Loubere et al., 2008 |

**Table A7. Indian Ocean $\delta^{13}C$ running mean and maximum anomalies.** Corresponding core, location, species used for $\delta^{13}C$ record, tier, and reference are listed.

| Core | Latitude | Longitude | Species | Tier | Running Mean Anomaly (‰) | Maximum Anomaly (‰) | Reference |
|---|---|---|---|---|---|---|---|
| WIND 28K | -10.2 | 51.8 | *N. dutertrei* | 1 | -0.17 | -0.25 | Kiefer et al., 2006 |
| 905 | 10.5 | 51.6 | *G. bulloides* | 2 | -0.39 | -0.55 | Jung et al., 2009 |

REFERENCES

Abrantes, F., Baas, J., Haflidason, H., Rasmussen, T. L., Klitgaard, D., Loncaric, N., Gaspar, L. (1998), Sediment fluxes along the northeastern European Margin: inferring hydrological changes between 20 and 8 kyr, *Mar. Geol., 152,* 7–23.

Adkins J. F. (2013), The role of deep ocean circulation in setting glacial climates. *Paleoceanography, 28,* 539-61.

Anderson, R. F., Ali, S., Bradtmiller, L. I., Nielsen, S. H. H., Fleisher, M.Q., Anderson, B. E., Burckle, L. H. (2009), Wind-driven upwelling in the Southern Ocean and the deglacial rise in atmospheric CO2. *Science, 323,* 1443-8.

Barnola, J. M., Raynaud, D., Korotkevich, Y. S., Lorius, C. (1987), Vostok ice core provides 160,000-year record of atmospheric CO2. *Nature, 329,* 408-14.

Bauska, T. K., Baggenstos, D., Brook, E. J., Mix, A. C., Marcott, S. A., Petrenko, V. V., Schaefer, H., Severinghaus, J. P., Lee, J. E. (2016), Carbon isotopes characterize rapid changes in atmospheric carbon dioxide during the last deglaciation. *Proceedings of the National Academy of Sciences, 113(13),* 3465-3470.

Bostock, H. C., Opdyke, B. N., Gagan, M. K., Fifield, L. K. (2004), Carbon isotope evidence for changes in antarctic intermediate water circulation and ocean ventilation in the southwest pacific during the last deglaciation. *Paleoceanography, 19,* 1-15.

Bouttes, N., Roche, D. M., Paillard, D. (2012), Systematic study of the impact of fresh water fluxes on the glacial carbon cycle. *Climate of the Past, 8(2),* 589-607.

Broecker, W.S. (1982), Ocean chemistry during glacial time. *Geochim. Cosmochim. Acta., 46,* 1689-705.

Broecker, W.S. and Maier-Reimer, E. 1992. The influence of air and sea exchange on the carbon isotope distribution in the sea. Global Biogeochem Cycles 6(3):315-20.

Broecker, W. S., Peng, T. H. (1974), Gas exchange rates between air and sea, *Tellus, 26,* 21-35.

Cannariato, K. G., and Ravelo, A. C. (1997), Pliocene-pleistocene evolution of eastern tropical pacific surface water circulation and thermocline depth. *Paleoceanography, 12(6),* 805-20.

Carter, L., Manighetti, B., Ganssen, G., Northcote, L. (2008), Southwest pacific modulation of abrupt climate change during the antarctic cold reversal-younger dryas. *Palaeogeogr. Palaeoclimatol. Palaeoecol., 260,* 284-98.

Charles, C.D., Lynch-Stieglitz, J., Ninnemann, U.S., Fairbanks, R.G. (1996) Climate connections between the hemisphere revealed by deep sea sediment core/ice core correlations. *Earth Planet Sci. Lett., 142,* 19-27.

Chen, T., Robinson, L. F., Burke, A., Southon, J., Spooner P, Morris, P. J., Ng, H. C. (2015), Synchronous centennial abrupt events in the ocean and atmosphere during the last deglaciation. *Science, 349,* 1537-41.

Chiessi, C. M., Mulitza, S., Mollenhauer, G., Silva, J.B., Groeneveld, J., Prange, M. (2015), Thermal evolution of the western south Atlantic and the adjacent continent during termination 1. *Climate of the Past, 11,* 915-29.

Clark, P. U., McCabe, A. M., Mix, A. C., Weaver, A. J. (2004), Rapid rise of sea level 19,000 years ago and its global implications. *Science, 304(5674),* 1141-4.

Curry, W.B., Crowley, T. J. (1987), The d13C of equatorial Atlantic surface waters: Implications for ice age pCO2 levels. *Paleoceanography, 2,* 489-517.

Curry, W. B., Duplessy, J. C., Labeyrie, L. D., Shackleton, N. J. (1988), Changes in the distribution of d13C of deep water SCO2 between the last glaciation and the holocene. *Paleoceanography, 3,* 317-41.

d'Orgeville, M., Sijp, W. P., England, M. H., Meissner, K. J. (2010), On the control of glacial-interglacial atmospheric CO2 variations by the southern hemisphere westerlies. *Geophys. Res. Lett. 37(21).*

Dürkoop, A., Hale, W., Mulitza, S., Pätzold, J., Wefer, G. (1997), Late quaternary variations of sea surface salinity and temperature in the western tropical atlantic: Evidence from d18O of globigerinoides sacculifer. *Paleoceanography, 12(6),* 764-72.

Elderfield, H., Vautravers, M., Cooper, M. (2002), The relationship between shell size and Mg/Ca, Sr/Ca, D18O, and D13C of species of planktonic foraminifera. *Geochemistry, Geophysics, Geosystems, 3(8),* 1-13.

Freudenthal, T., Meggers, H., Henderiks, J., Kuhlmann, H., Moreno, A., and Wefer, G. (2002), Upwelling intensity and filament activity off Morocco during the last 250,000 years. *Deep Sea Res. II, 49,* 3655–3674.

Gherardi, J., Labeyrie, L., Nave, S., Francois, R., McManus, J. F., Cortijo, E. (2009), Glacial-interglacial circulation changes inferred from 231Pa/230Th sedimentary record in the north Atlantic region. *Paleoceanography, 24(2).*

Govil, P., Naidu, P. D. (2010), Evaporation-precipitation changes in the eastern arabian sea for the last 68 ka: Implications on monsoon variability. *Paleoceanography 25(1).*

Hertzberg, J. E., Lund, D. C., Schmittner, A., Skrivanek, A. L. (submitted). Evidence for a Biological Pump Driver of Atmospheric CO2 Rise during Heinrich Stadial 1. *Nature Geoscience*.

Hodell, D. A., Venz, K. A., Charles, C. D., Ninnemann, U. S. (2003), Pleistocene vertical carbon isotope and carbonate gradients in the south atlantic sector of the southern ocean. *Geochem. Geophys. Geosyst., 4(1).*

Howard, W. R. and Prell, W. L. (1992), Late quaternary surface circulation of the southern indian ocean and its relationship to orbital variations. *Paleoceanography 7(1)*, 79-117.

Ito, T., Follows, M. J. (2005), Preformed phosphate, soft tissue pump and atmospheric CO2. *J. Mar. Res., 63(4)*, 813-39.

Johnstone, H. J. H., et al. (2014), Calcite saturation, foraminiferal test mass, and Mg/Ca-based temperatures dissolution corrected using XDX - A 150 ka record from the western Indian ocean. *Geochemistry, Geophysics, Geosystems, 15(3)*, 781-97.

Jung, S. J. A. and Sarnthein, M. (2003a), Stable isotope data of sediment cores GIK23419-8, PANGAEA, doi:10.1594/PANGAEA.112916.

Jung, S. J. A. and Sarnthein, M. (2003c), Stable isotope data of sediment cores GIK23415-9, PANGAEA, doi:10.1594/PANGAEA.112912.

Jung, S. J. A. and Sarnthein, M. (2003d), Stable isotope data of sediment cores GIK23418-8, PANGAEA, doi:10.1594/PANGAEA.112915.

Jung, S. J. A. and Sarnthein, M. (2004a), Stable isotope analysis of foraminifera from sediment cores GIK17049-6, PANGAEA, doi:10.1594/PANGAEA.112908.

Jung, S. J. A., Kroon, D., Ganssen, G., Peeters, F., and Ganeshram, R. (2009), Enhanced Arabian Sea intermediate water flow during glacial North Atlantic cold phases. *Earth Planet. Sc. Lett., 280*, 220–228.

Kiefer, T., McCave, I. N., Elderfield, H. (2006), Antarctic control on tropical Indian ocean sea surface temperature and hydrography. *Geophys. Res. Lett., 33(24)*.

Kohfeld, K. E., Graham, R. M., de Boer, A. M., Sime, L. C., Wolff, E. W., Le Quéré, C., Bopp, L. (2013), Southern hemisphere westerly wind changes during the last glacial maximum: Paleo-data synthesis. *Quat Sci Rev, 68*, 76-95.

Kroopnick, P. M. (1985), The distribution of 13C of SCO2 in the world oceans. Deep Sea Research Part A, *Oceanographic Research Papers, 32(1)*, 57-84.

Koutavas, A. and Lynch-Stieglitz, J. (2003), Glacial-interglacial dynamics of the eastern equatorial pacific cold tongue-intertropical convergence zone system reconstructed from oxygen isotope records. *Paleoceanography, 18(4)*, 13,1 - 13-16.

Labeyrie, L. (1996), Quaternary paleoceanography: unpublished stable isotope records. IGBP PAGES/World Data Center for Paleoclimatology Data Contribution Series #1996-036, NOAA/NGDC Paleoclimatology Program, Boulder, Colorado, USA.

Labeyrie, L., Vidal, L., Cortijo, E., Paterne, M., Arnold, M., Duplessy, J.-C., Vautravers, M., Labracherie, M., Duprat, J., Turon, J. L., Grousset, F., and Van Weering, T. (1995), Surface and deep hydrology of the Northern Atlantic Ocean during the last 150000 years. *Phil. Trans. Royal Soc. London, B, 348*, 255–264.

Li, T., Zhao, J., Nan, Q., Sun, R., Yu, X. (2011), Palaeoproductivity evolution in the centre of the western pacific warm pool during the last 250 ka. *J Quat Sci, 26(5)*, 478-84.

Li, T., Liu, Z., Hall, M. A., Saito, Y., Berne, S., Cang, S., Cheng, Z. (2002), A broad deglacial d13C minimum event in planktonic foraminiferal records in the okinawa trough. *Chin Sci Bull, 47(7)*, 599-603.

Lisiecki, L. E., Raymo, M. E. (2005), A pliocene-pleistocene stack of 57 globally distributed benthic d18O records. *Paleoceanography, 20(2)*, 1.

Loubere, P. and Bennett, S. (2008), Southern ocean biogeochemical impact on the tropical ocean: Stable isotope records from the pacific for the past 25,000 years. *Global Planet Change, 63(4)*, 333-40.

Loubere, P., Fariduddin, M., Richaud, M. (2011), Glacial marine nutrient and carbon redistribution: Evidence from the tropical ocean. *Geochem Geophys Geosyst, 12(8)*.

Lowry, R. K., Machin, P., and Cramer, R. N. (1994), BOFS North Atlantic Data Set. Oceanographic data collected during the North Atlantic cruises of the NERC Biogeochemical Ocean Flux Study (1989–1991): a UK contribution of JGOFS, Natural Environmental Research Council, British Oceanographic Data Centre, Merseyside, UK.

Lund, D. C., Adkins, J. F., Ferrari, R. (2011), Abyssal atlantic circulation during the last glacial maximum: Constraining the ratio between transport and vertical mixing. *Paleoceanography 26(1).*

Lund, D. C., Curry, W. (2006), Florida current surface temperature and salinity variability during the last millennium. *Paleoceanography 21(2)*.

Lund, D. C., Tessin, A. C., Hoffman, J. L., Schmittner, A. (2015), Southwest atlantic water mass evolution during the last deglaciation. *Paleoceanography, 30(5)*, 477-94.

Lynch-Stieglitz, J. et al. (2005), Deep Pacific CaCO3 compensation and glacial–interglacial atmospheric CO2. *Earth and Planetary Sciences Letters, 231(3)*, 317-336.

Lynch-Stieglitz, J., Curry, W., and Oppo, D. (2006), Meridional overturning circulation in the South Atlantic at the last glacial maximum. *Geochem. Geophys. Geosyst., 7,* doi:10.1029/2005GC001226.

Marcott, S. A., Bauska, T. K., Buizert, C., Steig, E. J., Rosen, J. L., Cuffey, K. M., Fudge, T. J., Severinghaus, J. P., Ahn, J., Kalk, M. L., et al. (2014), Centennial-scale changes in the global carbon cycle during the last deglaciation. *Nature, 514(7524),* 616-9.

Martinez-Mendez, G., Zahn, R., Hall, I. R., Peeters, F. J. C., Pena, L. D., Cacho, I., Negre, C. (2010), Contrasting multiproxy reconstructions of surface ocean hydrography in the agulhas corridor and implications for the agulhas leakage during the last 345,000 years. *Paleoceanography, 25(4)*.

McCave, I. N., Carter, L., Hall, I. R. (2008), Glacial-interglacial changes in water mass structure and flow in the SW Pacific Ocean. *Quaternary Science Reviews 27(19-20),*1886-908.

McManus, J. F., Francois, R., Gherardl, J., Kelgwin, L., Drown-Leger, S. (2004), Collapse and rapid resumption of atlantic meridional circulation linked to deglacial climate changes. *Nature, 428(6985),* 834-7.

Menviel, L., Timmermann, A., Mouchet, A., Timm, O. (2008), Meridional reorganizations of marine and terrestrial productivity during heinrich events. *Paleoceanography 23(1)*.

Monnin, E., Indermühle, A., Dällenbach, A., Flückiger, J., Stauffer, B., Stocker, T. F., Raynaud, D., Barnola, J. (2001), Atmospheric CO2 concentrations over the last glacial termination. *Science, 291(5501),* 112-4.

Neftel, A., Oeschger, H., Schwander, J., Stauffer, B., Zumbrunn, R. (1982), Ice core sample measurements give atmospheric CO2 content during the past 40,000 yr. *Nature, 295(5846),* 220-3.

Ninnemann, U. S. and Charles, C. D. (1997), Regional differences in quaternary subantarctic nutrient cycling: Link to intermediate and deep water ventilation. *Paleoceanography, 12(4)*, 560-7.

Obata, A. (2007), Climate-carbon cycle model response to freshwater discharge into the North Atlantic. *Journal of Climate, 20(24)*, 5962-5976.

Oppo, D. W., Curry, W. B., McManus, J. F. (2015), What do benthic d13C and d18O data tell us about atlantic circulation during heinrich stadial 1? *Paleoceanography, 30(4)*, 353-68.

Oppo, D. W. and Fairbanks, R. G. (1989), Carbon isotope composition of tropical surface water during the past 22 000 years. *Paleoceanography 4(4)*, 333-51.

Ostermann, D. R. and Curry, W. B. (2000), Calibration of stable isotopic data: An enriched d18O standard used for source gas mixing detection and correction. *Paleoceanography, 15(3)*, 353-60.

Pahnke, K. and Zahn, R. (2005), Southern hemisphere water mass conversion linked with north atlantic climate variability. *Science, 307(5716)*, 1741-6.

Pahnke, K., Zahn, R., Elderfield, H., Schulz, M. (2003), 340,000-year centennial-scale marine record of southern hemisphere climatic oscillation. *Science, 301(5635)*, 948-52.

Patrick, A. and Thunell, R. C. (1997), Tropical pacific sea surface temperatures and upper water column thermal structure during the last glacial maximum. *Paleoceanography, 12(5)*, 649-57.

Pena, L. D., Cacho, I., Ferretti, P., Hall, M. A. (2008), EI niño-southern oscillation-like variability during glacial terminations and interlatitudinal teleconnections. *Paleoceanography, 23(3)*.

Petit, J. R., Jouzel, J., Raynaud, D., Barkov, N. I., Barnola, J., Basile, I., Bender, M., Chappellaz, J., Davis, M., Delaygue, G., et al. (1999), Climate and atmospheric history of the past 420,000 years from the vostok ice core, antarctica. *Nature, 399(6735)*, 429-36.

Pierre, C., Saliege, J. F., Urrutiaguer, M. J., and Giraudeau, J. (2001), Stable isotope record of the last 500 k.y. at Site 1087 (Southern Cape Basin), *Proc. Ocean Drill. Program Sci. Results, 175*.

Rickaby, R. E. M. and Elderfield, H. (1999), Planktonic foraminiferal Cd/Ca: Paleonutrients or paleotemperature? *Paleoceanography, 14(3)*, 293-303.

Romahn, S., MacKensen, A., Groeneveld, J., Pätzold, J. (2014), Deglacial intermediate water reorganization: New evidence from the indian ocean. *Clim Past, 10(1)*, 293-303.

Sagawa, T., Yokoyama, Y., Ikehara, M., Kuwae, M. (2012), Shoaling of the western equatorial pacific thermocline during the last glacial maximum inferred from multispecies temperature reconstruction of planktonic foraminifera. *Palaeogeogr, Palaeoclimatol, Palaeoecol, 346-347*, 120-9.

Sarnthein, M. (1994), Changes in east atlantic deepwater circulation over the last 30 000 years: Eight time slice reconstructions. *Paleoceanography, 9(2)*, 209-67.

Schmidt, G. A., Bigg, G. R., Rohling, E. J. (1999), "Global Seawater Oxygen-18 Database - v1.21" http://data.giss.nasa.gov/o18data/

Schmitt, J., Schneider, R., Elsig, J., Leuenberger, D., Lourantou, A., Chappellaz, J., Köhler, P., Joos, F., Stocker, T. F., Leuenberger, M., et al. (2012), Carbon isotope constraints on the deglacial CO2 rise from ice cores. *Science, 336(6082)*, 711-4.

Schmittner, A. (2005), Decline of the marine ecosystem caused by a reduction in the atlantic overturning circulation. *Nature, 434(7033)*, 628-33.

Schmittner, A., Galbraith, E. D. (2008), Glacial greenhouse-gas fluctuations controlled by ocean circulation changes. *Nature, 456(7220)*, 373-376.

Schmittner, A. and Lund, D. C. (2015), Early deglacial atlantic overturning decline and its role in atmospheric CO2 rise inferred from carbon isotopes (d13C). *Clim Past 11(2)*, 135-52.

Schneider, R., Dahmke, A., Kolling, A., Muller, P. J., Schulz, H. D., Wefer, G. (1992), Strong deglacial minimum in the d13C record from planktonic foraminifera in the benguela upwelling region: Palaeoceanographic signal or early diagenetic imprint? *Upwelling Systems: Evolution since the Early Miocene*, 285-97.

Shackleton, N. J. and Pisias, N. G. (1985), Atmospheric carbon dioxide, orbital forcing, and climate. The Carbon Cycle and Atmospheric CO2, Natural Variations Archean to Present.Chapman Conference Papers, 1984, 303-17.

Shackleton, N. J., Le, J., Mix, A., Hall, M. A. (1992), Carbon isotope records from pacific surface waters and atmospheric carbon dioxide. *Quat Sci Rev, 11(4)*, 387-400.

Shakun, J. D., Clark, P. U., He, F., Marcott, S. A., Mix, A. C., Liu, Z., Otto-Bliesner, B., Schmittner, A., Bard, E. (2012), Global warming preceded by increasing carbon dioxide concentrations during the last deglaciation. *Nature, 484(7392)*, 49-54.

Sigman, D. M. and Boyle, E. A. (2000), Glacial/interglacial variations in atmospheric carbon dioxide. *Nature, 407(6806)*, 859-69.

Sigman, D. M., Hain, M. P., Haug, G. H. (2010), The polar ocean and glacial cycles in atmospheric CO2 concentration. *Nature, 466(7302)*, 47-55.

Sikes, E. L. and Keigwin, L. D. (1994), Equatorial Atlantic sea surface temperature for the last 30 kyr: A comparison of Uk37, delO18 and foraminiferal assemblage temperature estimates. *Paleoceanogr., 9*, 31–45.

Spero, H. J., Bijma, J., Lea, D. W., Bernis, B. E. (1997), Effect of seawater carbonate concentration on foraminiferal carbon and oxygen isotopes. *Nature, 390(6659)*, 497-500.

Spero, H. J. and Lea, D. W. (1993), Intraspecific stable isotope variability in the planktic foraminifera globigerinoides sacculifer: Results from laboratory experiments. *Mar Micropaleontol 22(3)*, 221-34.

Spero, H. J. and Lea, D. W. (1996), Experimental determination of stable isotope variability in globigerina bulloides: Implications for paleoceanographic reconstructions. *Mar Micropaleontol 28(3-4)*, 231-46.

Spero, H. J. and Lea, D. W. (2002), The cause of carbon isotope minimum events on glacial terminations. *Science, 296(5567)*, 522-5.

Spero, H. J., Mielke, K. M., Kalve, E. M., Lea, D. W., Pak, D. K. (2003), Multispecies approach to reconstructing eastern equatorial pacific thermocline hydrography during the past 360 kyr. *Paleoceanography, 18(1)*, 22,1-22-16.

Stommel H. (1961), Thermohaline convection with two stable regimes of flow. *Tellus, 13*, 224-30.

Stott, L., Poulsen, C., Lund, S., Thunell, R. (2002), Super ENSO and global climate oscillations at millennial time scales. *Science, 297(5579)*, 222-6.

Thunell, R. C., Miao, Qingmin, Calvert, S. E., Pedersen, T. F. (1992), Glacial holocene biogenic sedimentation patterns in the south china sea: Productivity variations and surface water pCO2. *Paleoceanography, 7(2)*, 143-62.

Toggweiler, J. R. (1999), Variation of atmospheric CO2 by ventilation of the ocean's deepest water. *Paleoceanography, 14(5)*, 571-88.

Toggweiler, J. R., Russell, J. L., Carson, S. R. (2006), Midlatitude westerlies, atmospheric CO2, and climate change during the ice ages. *Paleoceanography, 21(2)*.

Tschumi, T., Joos, F., Parekh, P. (2008), How important are southern hemisphere wind changes for low glacial carbon dioxide? A model study. *Paleoceanography, 23(4)*.

Venz, K. A., Hodell, D. A., Stanton, C., Warnke, D. A. (1999), A 1.0 myr record of glacial north atlantic intermediate water variability from ODP site 982 in the northeast atlantic. *Paleoceanography, 14(1)*, 42-52.

Veres, D., Bazin, L., Landais, A., Toyé Mahamadou Kele, H., Lemieux-Dudon, B., Parrenin, F., Martinerie, P., Blayo, E., Blunier, T., Capron, E., et al. (2013). The antarctic ice core chronology (AICC2012): An optimized multi-parameter and multi-site dating approach for the last 120 thousand years. *Climate of the Past 9(4)*, 1733-48.

Völker, C. and Köhler, P. (2013), Responses of ocean circulation and carbon cycle to changes in the position of the southern hemisphere westerlies at last glacial maximum. *Paleoceanography, 28(4)*, 726-39.

Webb, R. S., Rind, D. H., Lehman, S. J., Healy, R. J., Sigman, D. (1997), Influence of ocean heat transport on the climate of the last glacial maximum. *Nature, 385(6618)*, 695-9.

Zarriess, M., Johnstone, H., Prange, M., Steph, S., Groeneveld, J., Mulitza, S., MacKensen, A. (2011). Bipolar seesaw in the northeastern tropical atlantic during heinrich stadials. *Geophys Res Lett 38(4)*.

Zhao, M., Beveridge, N. A. S., Shackleton, N. J., Sarnthein, M., and Eglinton, G. (1995), Molecular stratigraphy of cores off northwest Africa: Sea surface temperature history over the last 80 ka, *Paleoceanogr., 10*, 661–675.